Stony Brook University

Characterization of Dislocations Structures and Properties in Silicon Carbide Bulk Crystals and Epilayers

A Thesis Presented

by

Ning Zhang

to

The Graduate School

in Partial Fulfillment of the

Requirements

for the Degree of

Master of Science

in

Materials Science and Engineering

Stony Brook University

May 2009

Stony Brook University

The Graduate School

Ning Zhang

We, the thesis committee for the above candidate for the

Master of Science degree, hereby recommend

acceptance of this thesis.

Michael Dudley – Thesis Advisor
Professor, Department of Materials Science and Engineering

Jonathan C. Sokolov
Professor, Department of Materials Science and Engineering

Xianrong Huang
Associate Physicist, National Synchrotron Light Source II
Brookhaven National Laboratory

This thesis is accepted by the Graduate School

Lawrence Martin
Dean of the Graduate School

Abstract of the Thesis

Characterization of Dislocations Structures and Properties in Silicon Carbide Bulk Crystals and Epilayers

by

Ning Zhang

Master of Science

in

Materials Science and Engineering

Stony Brook University

2009

This report presents some preliminary studies of defects structures and properties in silicon carbide (SiC) bulk crystals and epilayers. The background, polytypism, properties and applications of silicon carbide are introduced. Current understandings of defect structures in SiC are reviewed, including Micropipes (MPs), threading screw dislocations (TSDs), threading edge dislocations (TEDs), basal plane dislocations (BPDs), stacking faults (SFs) and low angle grain boundaries (LAGDs). Recent observations of these defects and their behaviors during growth are presented as following:

I) Investigation of the influence of substrate surface scratches on the quality of chemical vapor deposition (CVD) grown 4H-SiC homo-epitaxial layers. Monochromatic Synchrotron X-ray Topography (MSXT) and KOH etching images suggest that the scratches on the substrate surface act as a dislocation nucleation center during the growth. Various kinds of dislocations were observed to nucleate at the scratch, including TED-TED pairs, TED-BPD pairs, pairs of opposite sign screw dislocations and carrot defects. The models are presented for possible mechanisms of dislocation nucleation at the scratch. Further studies show that such effect and mechanism can also be applied to the physical vapor transpor (PVT) growth of bulk SiC crystals.

II) Investigation of the formation mechanism of the dislocation half loop arrays (HLAs) in 4H-SiC homo-epitaxial layers. The HLAs have been studied using a combination of MSXT and Ultraviolet Photoluminescence (UVPL). A model is presented for the formation mechanism of dislocation HLAs formed during the epitaxial growth. The reorientation during glide of the formerly screw character surface intersections of threading segments of BPD render them susceptible to conversion into sessile TED which subsequently pin the motion of the BPD. Continued glide during further growth enables parts of the mobile BPD to escape through the surface leaving arrays of half loops

comprising two TEDs and a short BPD segment with significant edge component. The behavior of the arrays under UV excitation is consistent with this model.

III) Development of a strain/stress mapping technique in single crystals. Synchrotron white beam x-ray reticulography has been used to quantitatively map the residual strain/stress in SiC wafers. The basic principle of our study is that there exists a relationship between the stress state in a crystal and the local lattice plane orientation and that this relationship can be exploited in order to determine the full strain tensor as a function of position inside the crystal. The stress in a region of a commercial 4*H* silicon carbide wafer has been studied using this technique and the results are discussed.

Table of Contents

List of Acronyms

BPD	basal plane dislocation
CVD	chemical vapor deposition
HLA	half loop arry
LAGB	low angle grain boundary
MP	micropipe
MBXT	monochromatic beam x-ray topography
PD	partial dislocation
PVT	physical vapor transport
REDG	recombination enhanced dislocation glide
SF	stacking fault
SWBXT	synchrotron white beam x-ray topography
TED	threading edge dislocation
TSD	threading screw dislocation
XRT	x-ray topography

List of Figures

List of Tables

1. Introduction

Silicon carbide (SiC) is steadily replacing conventional semiconductor materials, e.g., silicon (Si) and gallium arsenide (GaAs), under certain extreme applications due to its outstanding properties such as high thermal conductivity, high breakdown voltage and high saturated electron drift velocity. The thermal conductivity of SiC is ~2 times higher than Si; the breakdown field is ~18.5 times the one of Si and the saturated electron drift velocity is twice that of the Si. The comparison of some properties between Si, *4H*-SiC and *6H*-SiC is listed in Table 1.

Table 1. Comparison of the properties between Si, *4H*-SiC and *6H*-SiC.

	E_g(eV)	T_w(K)	k (W/cm·K)	μ_e (cm^2/V·s)	μ_h (cm^2/V·s)	E_b (10^5V/cm)	V_s (10^7cm/s)
Si	1.12	410	1.31	1430	480	3	1
4H-SiC	3.26	1300	4.9	800	115	30	2
6H-SiC	3.03	1200	4.9	400	90	32	2

E_g: band gap; T_w: working temperature; k: thermal conductivity; μ_e: electron mobility; μ_h: hole mobility; E_b: breakdown field; V_s: saturated carrier velocity.

SiC is noted for its large number of polytypes. Up to now, more than 200 types of phases of SiC have been found. The first SiC structure found is *15R*: the same Si-C bilayer repeats every 15 layers with rhombohedral structure, which was labeled arbitrarily as type I; the second one is the hexagonal structure with six-layer repetition labeled as type II; the third one found is 4-layer hexagonal structure labeled as type III. The cubic structure was the fourth one to be discovered, which was naturally labeled as type IV. When more and more structures of SiC were found, it was impractical to keep using this labelling method. L. S. Ramsdell found that the basic unit that SiC is composed of (close-packed Si-C bilayer) is the same for the structures already found and possibly the same for the future structures. The polytypes come from different stacking sequences of the Si-C bilayers. Therefore, Ramsdell created a labelling principle to define the structures already discovered and even for potential structures to be discovered in the future.[1] The label is composed of a number which indicates the number of bilayers in the repeat unit followed by a letter C, H or R corresponding to cubic, hexagonal or rhombohedral. This is currently the most commonly used nomenclature for polytypes. The polytypes we are interested in are *4H* and *6H*-SiC. Although *3C*-SiC is a commonly observed polytype, we are not going to discuss in detail here because no large-size and high-quality *3C*-SiC can currently be grown.

Figure 1 shows the projection of the structures of *4H* and *6H*-SiC onto (11-20) plane. We can see that the stacking sequence is "ABCBABCB…" for *4H*-SiC and "ABCACBABCACB…" for *6H*-SiC.

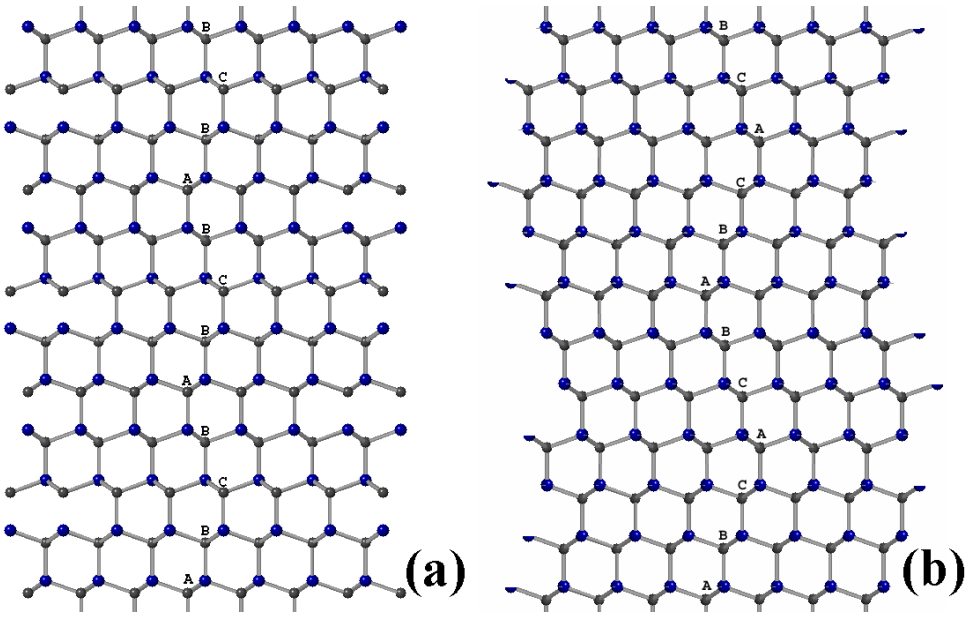

Figure 1. Projection of *4H*-SiC (a) and *6H*-SiC (b) structure into (11-20) plane. Small and large balls indicate C and Si atoms, respectively. The stacking sequences are "ABCB…" and "ABCACB…" for *4H* and *6H*-SiC, respectively.

The different stacking sequences of Si-C pairs are also related to the different densities of state of electrons and hence different properties. Knippenberg has demonstrated that, for short period structures such as *4H*, *6H*, *8H* and *15R*, they are controlled by the growth temperature, which means the short period structures can be explained by energy difference.[2] For long period structures, there is no evidence showing that they are thermodynamically stable. Frank[3] and Jagodzinski[4] presented two possible explanations from screw-dislocation and vibration entropy theory which are supported by experiments more than others, but experimental results that contradict these theories still exist. The influence of polarity of the substrates on the polytype is also reported: usually *6H*-SiC crystals are grown on the (0001) Si face of *6H*-SiC seed, whereas G. Augustine et al. found *4H*-SiC crystals were grown on the (0001) C face of *4H*-SiC crystal.[5]

SiC has extremely high melting point but it sublimes before it melts (see Figure 2. Phase diagram of C-Si. Peritectic point indicates that it is unfeasible to grow SiC from melt. for the phase diagram of C-Si system). Therefore, it is not feasible to grow SiC single crystals from the melt (e.g., Czochralski or Bridgman method). The commonly used technique for growing commercial SiC wafers is physical vapor transport (PVT, also called seeded modified Lely growth) and it was first carried out by Tairov and Tsvetkov in 1978.[6] In PVT growth, a growth temperature as high as 2300^{o}C is used and a temperature gradient is applied between the source (high-purity SiC powder) and seed. The high-purity SiC powder decomposes at the higher temperature end in the form of gaseous species and deposits as single crystals at the lower temperature end. The detailed growth process is not going to be discussed here and further information can be referred to a review by Chaussende *et al*.[7]

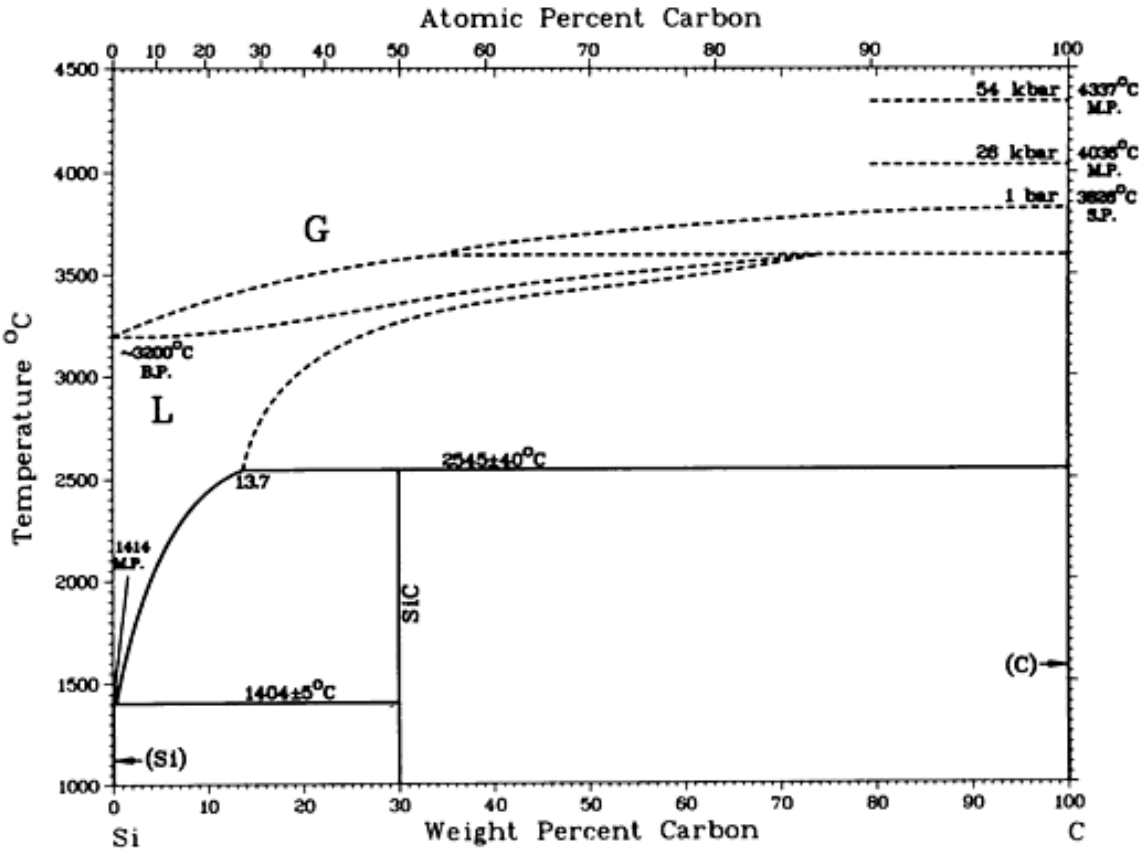

Figure 2. Phase diagram of C-Si.[8] Peritectic point indicates that it is unfeasible to grow SiC from melt.

1.1. Current Understanding of Defects Structure in SiC

Defects nucleated in SiC epilayers as well as in the substrates attract interest because some of them have been demonstrated to be detrimental to device performance. These defects include micropipes, elementary screw dislocations and stacking faults. It was found by Koga et al. for the first time in 1992 that p-n junction presented a very low breakdown voltage when micropipe was present.[9] This is clearly due to the open-core of micropipes. P. G. Neudeck et al. also found pre-avalanche reverse-bias point failures in most epitaxially grown p-n junction devices of 1mm^2 or larger in area.[10] Elementary screw dislocations, although not as detrimental as micropipes, could adversely affect the breakdown voltage of SiC devices and deteriorate the performance and reliability of SiC power devices. Highly localized breakdown current caused by micro-plasmas was observed by Neudeck et al.,[11] which results in 5-35% breakdown voltage reduction. The locations of observed breakdown micro-plasmas corresponded exactly to the locations of elementary screw dislocations identified by SWBXT mapping. The stacking fault is another defect that was found to degrade the SiC device performance. H. Lendenmann et al. reported an increase of voltage drop occurring over a period of hours or days under forward bias at moderate current densities in 4H-SiC p-n diodes.[12] Generation and expansion of stacking faults was also observed. In the following, different defects in SiC

including micropipes, threading screw dislocations, threading edge dislocations, basal plane dislocations, stacking faults and low angle grain boundaries are reviewed and discussed. It should be noted here that they are different types of defects but sometimes they are combined with each other, for example, low angle grain boundary might consist of basal plane dislocations, threading edge dislocations or screw dislocations.

1.1.1. Screw dislocations (SDs)

Screw dislocation has both Burgers vector and line direction along c axis. The screw dislocations observed in SiC can be divided into two categories: closed-core screw dislocations (threading screw dislocations, TSDs) and hollow-core screw dislocations (micropipes, MPs). In this report screw dislocations refer only to close-core screw dislocations unless noted. The most effective way to observe these SDs is back reflection X-ray topographs. They are observed to be white dots with different sizes in the X-ray topograph. Vetter et al.[13] observed in hexagonal SiC (4H and 6H) screw dislocations with Burgers vectors of magnitude two multiples of the c-lattice parameter or less are close-core SDs. Fig. 3 shows typical back reflection X-ray topograph and transmission X-ray topograph of a SiC crystal showing large number of screw dislocations (small white dots). One can see in back reflection geometry, screw dislocations show white dots with different sizes corresponding to different Burgers vectors and in transmission geometry screw dislocations serve as the junctions of BPDs (black lines).

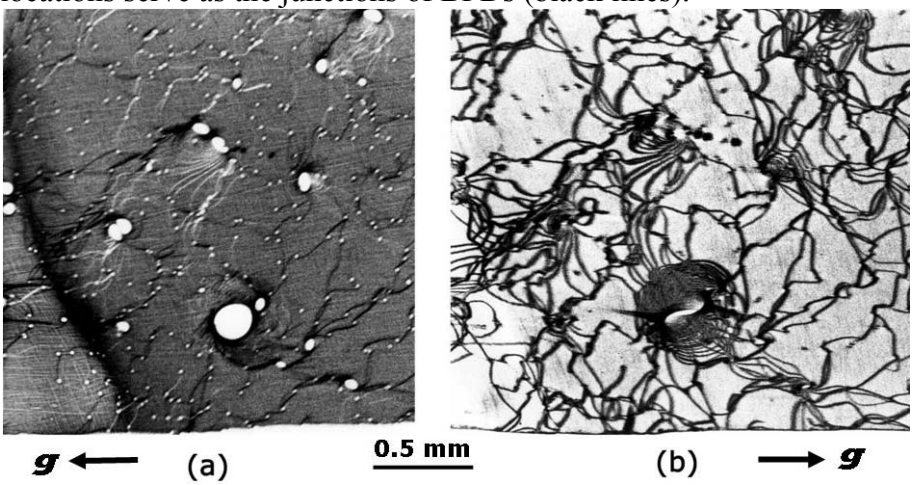

Figure 3. Typical back reflection X-ray topograph (a) and transmission X-ray topograph (b) showing SDs. Small white dots are elementary TSDs and large white dots are MPs. (after Vetter)

Replication of SDs, which threads the moving crystal-growth front or interface, is commonly seen. They are not produced by plastic deformation and probably they are related to nucleation faults[14] due to the large energy needed for screw dislocation formation. Dudley et al. reported that incorporation of inclusions resulted in a pair of micropipes with opposite Burgers vectors and this clearly accounts for one of the reasons for nucleation of screw dislocations. Sanchez et al.[15] found on on-axis epitaxy the density of SDs is a factor of 300 higher than off-axis epitaxy. They interpreted this phenomenon as the result of two-dimension nucleation: islands expand and coalesce with the neighboring islands, some of the bounding dislocations can have Burgers vector along c

axis and are possible sites for nucleation of SDs. Based on this model, SD density can be effectively reduced by step flow growth compared to 2D nucleation growth. This is due to the large number of steps existed on the vicinal surface seed used in step flow growth. The presence of large numbers of kinks provides the energetically stable sites for adatoms and the growth is going on by expanding the terraces. However, the c-cut seed results in very small unintentional misorientations which cause the nucleation of steps. SDs nucleate at those disordered misorientation sites. This explains the larger density of SDs in on-axis growth compared to off-axis growth. [15]

1.1.2. Micropipes (MPs)

The micropipe (MP) is the defect that has been discussed the most in SiC. The first topographic observation of the presence of MPs in SiC was done by Dudley et al. [16] As a result of their work, it is now commonly accepted that MP is pure screw dislocation with giant Burgers vector along c direction although some people claimed that MP is composed of mixed edge and screw type. [17] The contrast formed under $\vec{g} \cdot \vec{b} = 0$ has been successfully interpreted by the in-plane strains induced from the dislocation image force near the crystal surface.[18] The critical Burgers vectors for a hollow core screw dislocation are 2c and 3c for 6H and 4H SiC, respectively. [19, 20] The presence of the hollow core can be explained by Frank's theory to reduce the local strain energy of the micropipe. The diameter of the MP increases with the square of Burgers vector. The typical micropipe image recorded by back reflection SWBXT is in the form of a nearly circular black ring surrounding a white center (see large white dots in Fig. 3). [21] The Burgers vector of the MP can be determined by measuring the diameter of MP image in back reflection X-ray topography. [21] The physical shape of MPs is not round and they may show hexagonal shape or elongated hexagonal shape (Fig. 4). MP is the most detrimental defect for high power and high voltage devices because the MP will increase leakage current and reduce the breakdown voltage drastically.

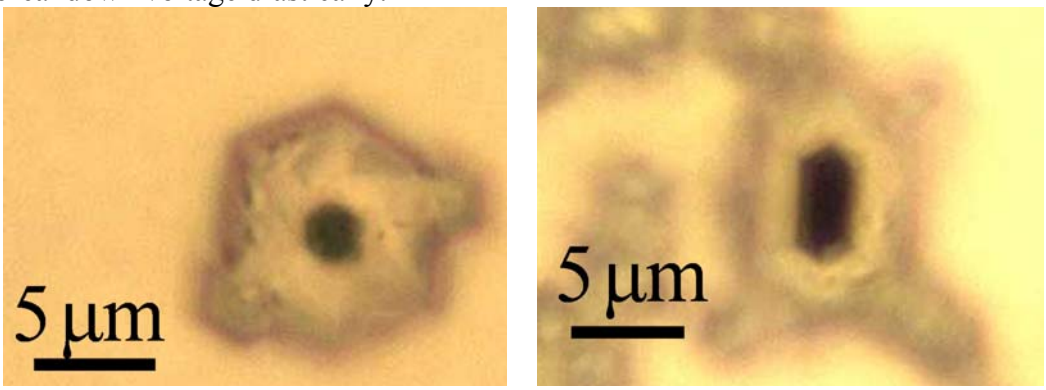

(a) (b)

Figure 4. Optical micrograph of two MPs after KOH etching. (a) hexagonal MP; (b) elongated hexagonal MP.

Inheritance of MPs from seed is commonly seen in growth of SiC. Also they may come from the relaxation of stresses from handling damage on the seed surface. Another possible reason to nucleate MPs is the relaxation of stresses arising from the incorporation of inclusions of solvent or impurity which can occur on the seed surface or

later during growth or equivalently imperfect lattice closure around such an inclusion. [22] Other nucleation mechanisms including heterogeneous phase[23] and hexagonal voids[24] were also proposed to explain the formation of MPs. However, there is no unanimous interpretation although they do not conflict with each other. Understanding the MP nucleation mechanism thoroughly so as to eliminate the MP completely remains a challenge for SiC researchers.

Based on dislocation theory, the extra energy that an imperfect crystal possesses compared to a perfect crystal is the strain energy of the dislocations. MPs can dissociate into small Burgers vector SDs to reduce the total strain energy. For close-core SD, this strain energy per unit length is $E_{SD} = \alpha G b^2$ where α is a constant, G is the shear modulus and b is the magnitude of Burgers vector. Assuming α is the same for each SD in SiC, the closed-core SDs with large Burgers vectors are tending to dissociate into elementary SDs based on the fact $(nb)^2 > nb^2$. Thus, once the hollow-core is filled, the MP cannot end and it favors dissociation into several elementary SDs. Filip et al. [25] reported the closure of 80% of the MPs with the diameter less than 5μm using liquid phase epitaxy.

1.1.3. Threading edge dislocations (TEDs)

Threading edge dislocations (TEDs) are pure edge type dislocations with Burgers vectors ($1/3<11\bar{2}0>$) perpendicular to their line directions (along c-axis). Threading edge dislocation is introduced by extra half ($1\bar{1}00$) habit plane. Contrast of TEDs is very close to the maximum resolution of white beam X-ray topography, but still it is discernible. Monochromatic beam X-ray topography has much better rsolution and has been used to reveal the detailed structure of TEDs (Fig. 5a). Chen has done the Burgers vectors analysis and image simulation in X-ray topograph for TEDs. [26] It matches the experimental topographs very well (shown in Fig. 5a). TEDs are mostly inherited from the substrate or converted from bent BPDs due to image force. [27] Ha et al.[28] also proposed the formation of TEDs due to prismatic plane slip. The TED is the reason for prismatic plane tilt and they are commonly seen in molten KOH etching aligning along the grain boundary (Fig. 5b). No negative influence of TEDs has been reported in SiC devices.

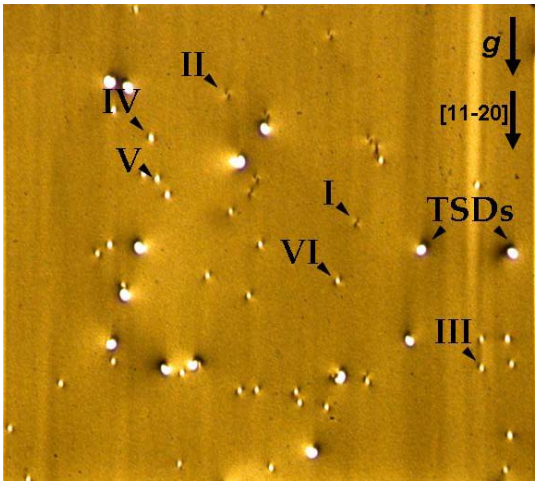

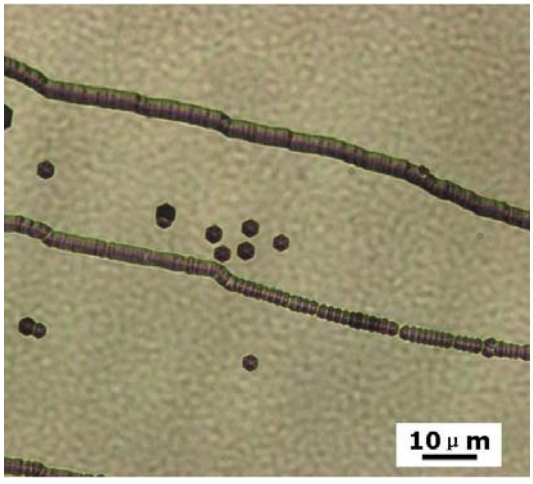

(a) (b)

Figure 5. (a) Grazing-incidence topograph of an off-axis SiC showing various images of TEDs. I-VI: six different types of images of TEDs observed in the topographs, corresponding to the six types of TEDs. (after Chen) (b) Alignment of TED etch pits along the grain boundary.

1.1.4. Basal plane dislocations (BPDs)

Basal plane dislocations (BPDs) are probably the defects with the highest density of all the dislocations that one can see from X-ray topographs. They usually show as black curved lines in the transmission topograph. Fig. 6 is the $[1\bar{1}20]$ transmission topograph of a Lely seed. A large number of curved basal plane dislocations shown as black lines can be seen. The BPDs lie in the basal plane (c plane) because the primary slip plane for 4H and 6H is the basal plane due to its largest inter-plane distance. These BPDs have Burgers vectors of $1/3<1\bar{1}20>$ type and they are edge, screw or mixed type depending on the angle between line direction and Burgers vector. BPDs form mostly to relax the stress caused by temperature gradients introduced during cooling down from growth temperature to room temperature. BPD is the reason for basal plane tilt low angle grain boundaries (see section 1.1.6).

BPDs in p-n diodes were observed to dissociate into two Shockley partials with a ribbon of stacking fault between them and expand. [12] This caused an increase of forward voltage drop. Electron-hole pair recombination was interpreted to provide the energy needed for dissociation and expansion. [29] Si-core partials are much more mobile than C-core partials due to lower bond energy and below certain temperature only Si-core partials can move. [30] Therefore, the Si-core partial dislocations move provided the energy by electron-hole pair recombination while C-core partial stays still. This is also to be discussed in section 1.1.5.

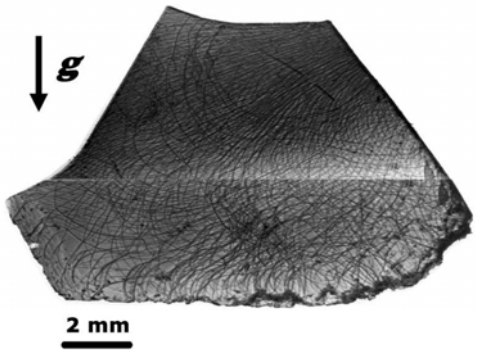

Figure 6. $[1\bar{1}20]$ transmission topograph of a 6H Lely seed showing BPDs as black curved lines.

1.1.5. Stacking faults (SFs)

Stacking faults (SFs) are planar defects and they mostly exist in the primary slip plane, which, for SiC, is {0001}. In principle, three types of SFs can exist in hexagonal

system. The first one is the intrinsic SF (I_1). It is formed by removal of a basal plane followed by slip of $1/3<10\bar{1}0>$ of the crystal above this fault to reduce the total energy. The second one is intrinsic SF (I_2) which is formed by the slip of $1/3<10\bar{1}0>$ in a perfect crystal. The last one is extrinsic SF (E) and it is produced by inserting an extra plane. Extra energy is needed to generate the SF and this is called the SF energy. It differs greatly for different polytypes. The stacking fault bounded by two Shockley partials is the most commonly seen SF and it is I_2 type. Hong et al. [31] reported the I_2 type stacking fault energy of 4H-SiC is 14.7±2.5mJ/m^2 and that of 6H-SiC is 2.9±0.6mJ/m^2. Dissociation of BPDs into Shockley partials are seldom seen in SWBXT although Vetter et al. [32] reported an unusual example in a Lely platelet. This is because the approximate equilibrium separation of two partial dislocations is

$$d = \frac{Gb^2}{4\pi\gamma}$$

based on the dislocation theory [33], where d is the distance between two partial dislocations, G is the shear modulus, b is the magnitude of the two partials and γ is the stacking faults energy. Based on this equation, the equilibrium separation of two Shockley partials is 0.03μm for 4H-SiC and 0.17μm for 6H-SiC provided the shear modulus of SiC is 200GPa. This is the reason why usually we could not see the dissociation of BPDs into Shockley partial dislocations in SWBXT because they are below the maximum resolution of SWBXT. But stacking faults could be observed when they expand given by the energy of electron-hole recombination in SiC device. When forward voltage is loaded, basal plane dislocations with Burgers vector $1/3<11\bar{2}0>$ were observed to dissociate into two Shockley partial dislocations of Burgers vectors $1/3<10\bar{1}0>$ and $1/3<01\bar{1}0>$. The Burgers vector is conserved by reaction $1/3<11\bar{2}0>\rightarrow 1/3<10\bar{1}0>+1/3<01\bar{1}0>$ with a ribbon of stacking fault between the two Shockley partials. The existed stacking faults were also found to expand through the motion of Si-cored partials under forward bias. [34] These Formation and expansion of basal plane stacking faults bounded by partial dislocations were interpreted as the reason for the degradation of forward voltage. [35, 36]

1.1.6. Low angle grain boundaries (GBs)

Usually low angle grain boundaries show as white or black bands depending on the misorientation sense. The schematic diagram of how grain boundary is recorded on the X-ray film is shown in Fig. 7. Diffracted X-ray beams from different domains overlap (show black line) or separate with each other (show white line). Quantitative X-ray topography indicates that the tilt angles associated with these boundaries are usually a few arcsecs. Grain boundaries are explained to consist of high density of defects which cause the domain misorientation.

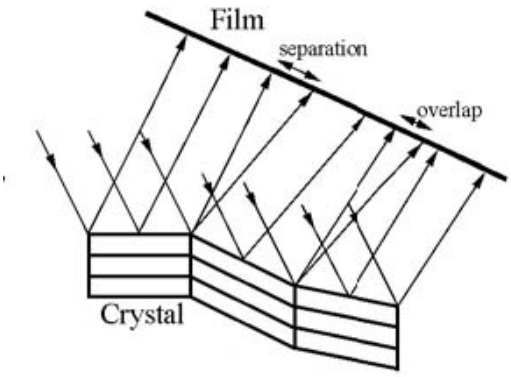

Figure 7. Schematic diagram shows grain boundary recording. (after Raghothamachar et al.[37])

Basically there are three types of misorientation of the domain walls which result in grain boundaries in SiC: one twist and two tilt. They come from three different rotations and are illustrated in Fig. 8. Fig. 8(a) shows a perfect crystal without any grain boundary. Imagine a plane (shaded in picture) separates the perfect crystal into two domains. There are three possible rotations. Any grain boundary is composed of one or more of them. These three rotations have axis along x, y or z (shown in Fig. 8(a)). They are named twisted boundary (Fig. 8(b)), basal plane tilt boundary (Fig. 8(c)) and prismatic plane tilt boundary (Fig. 8(d)), respectively.

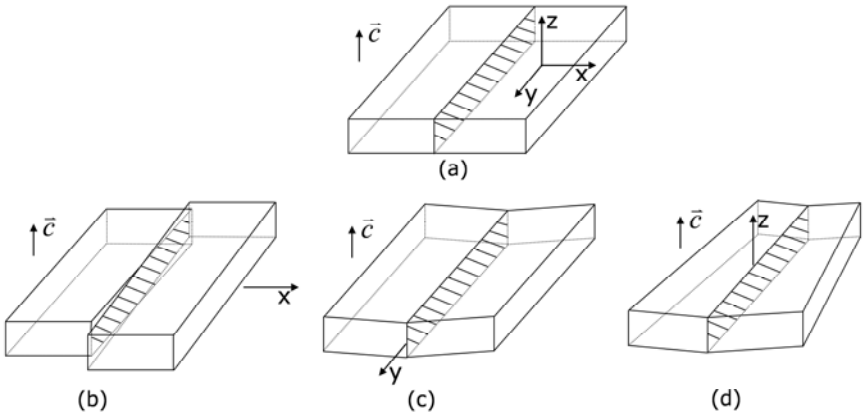

Figure 8. Schematic diagram showing three types of domain misorientation. (a) perfect crystal; (b) twisted grain boundary; (c) basal plane tilt boundary; (d) prismatic plane tilt boundary.

Different mechanisms explain the formation of different boundaries in SiC. S. Wang reported the micropipes aligning along a straight line are probably related to the domain twist. [38] Pile-up of basal plane dislocations is frequently seen in the topographs of grain boundaries. The BPDs lie in the domain wall plane and their Burgers vectors, which lie in the c plane, are perpendicular to their line directions. These BPDs result in the tilting of basal plane and basal plane tilt boundary forms. [39] Another type of domain wall misorientation comes from prismatic plane tilt which probably comes from the nucleation of threading edge dislocation. These TED lines are along the c axis (or at a

small angle tilt) and their Burgers vectors stay in the c plane. The alignment of these TEDs comes into being because their energy is minimized when they align along the line perpendicular to their Burgers vectors.

1.2. Motivation

SiC material has been facing serious issues related to various defects existing in the substrates and epilayers, such as MPs, TSDs, TEDs, BPDs, LAGBs consisting of a mixture of defects and SFs. [40-42] MPs are device-killing defects due to the hollow-core associated with them. [43] TSDs play a critical role in maintaining the desired polytype promoting spiral step-flow growth. However, they have been found to degrade device performance, reducing the breakdown voltage by 5-35%. [44] In addition, the forest of TSDs in the as-grown crystal poses a significant barrier which creates a pinning effect on the glide of the BPDs either during growth or post-growth cooling, leading to localized higher densities of BPDs. [45] TEDs play critical roles in the formation of LAGBs and they are also often observed to be converted from BPDs during CVD growth. Unconverted BPDs have been observed to be dissociated into partial dislocations and degrade the device performance. The interactions between the advancing partial dislocations and threading dislocations can lead to complex web of dislocations in SiC bipolar devices. Various extended defects (carrot defects, triangular defects) have also been observed to pose negative effects on the device performance. Therefore, if one is to be able to exert some control over the defect configurations encountered, this urgently requires a detailed understanding of the observed defect structures and their behavior and origins in SiC bulk crystals, epilayers and devices. Thus the primary motivation for our research in this area is to facilitate the development of strategies to either reduce the densities of the defects or completely eliminate them so as to mitigate their deleterious effects on device performance.

2. Experimental

2.1. Synchrotron X-ray Topography

Synchrotron x-ray topography (XRT) in our studies was done at the National Synchrotron Light Source (NSLS), Beamline X19C and at the Advanced Photon Source (APS), Beamline XOR-33BM/UNI-CAT. White beam XRT was carried out at NSLS and monochromatic XRT was carried out at the APS. The direct white beam from the storage ring is used at the NSLS and the maximum beam size at the sample is approximately 7 × 40 mm^2. The vertical divergence angle is $mc^2/E \approx 0.18$ mrad (m is the mass of the electron, c is the velocity of the light and E is the electron energy). In APS, the white beam is monochromatized by two cooled parallel Si(111) crystals and the x-ray energy is tunable between 2.4 – 40 keV. The schematic experimental setting-ups at NSLS and APS are illustrated in Figure 9

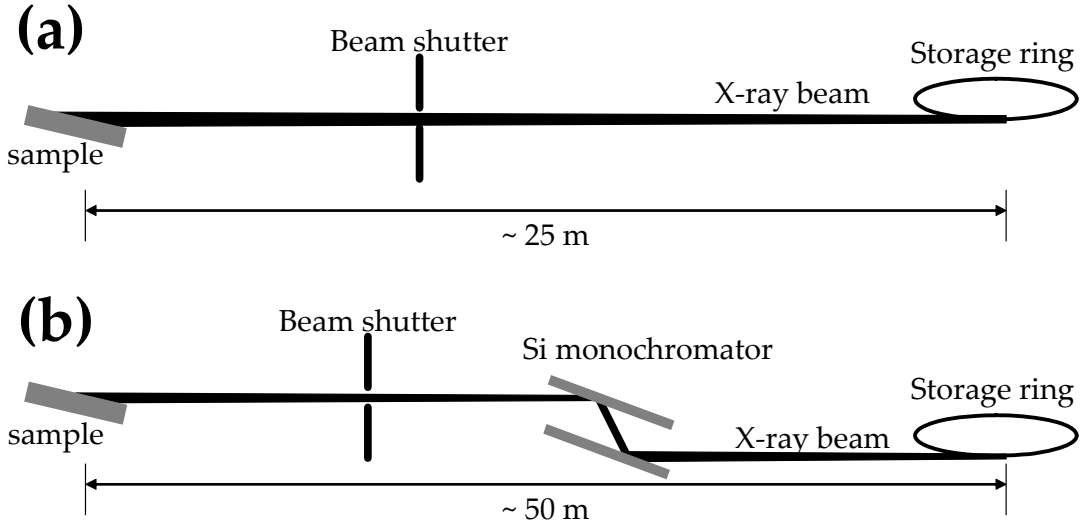

Figure 9. Schematics showing the experimental setting-ups at NSLS (a) and APS (b).

Mainly three geometries are used in our studies. The schematics of the three geometries are illustrated in Figure 10. The first one (Figure 10 (a)) is the transmission geometry, also called Laue geometry. In the transmission mode, the x-ray beam passes through the sample and the topographs recorded reveal the bulk defect information. In grazing-incidence reflection (Figure 10 (b)), a very small incident angle is used (typically 2^o) and the (11-28) or (11-2.12) reflection is recorded. Grazing-incidence is carried out because of the low penetration depth of x-ray beam in such geometry, which is particularly good for the studies of epilayers. The penetration depth can be tuned by rotating the sample along the reflection vector, or by simply adjusting the incident angle (the wavelength should be accordingly adjusted, of course). In back-reflection geometry (Figure 10 (c)), a large Bragg angle is used for basal plane reflection (000l) (typically 80^o). The screw dislocations along c-axis and the basal plane dislocations within the penetration depth of x-rays can be clearly recorded. The wavelength satisfying Bragg condition is automatically selected in white beam x-ray topography while in

monochromatic XRT, the energy of x-ray beam has to be pre-set to satisfy the diffraction condition.

Diffracted images are recorded on Agfa Structurix D3-SC, Ilford L4 nuclear plate, or VRP-M holographic films, depending on the resolution needed. Exposure time depends on the actual geometry and recording media and it varies between a few seconds and two hours. Kodak D19 developer and fixer were used to process the exposed emulsions.

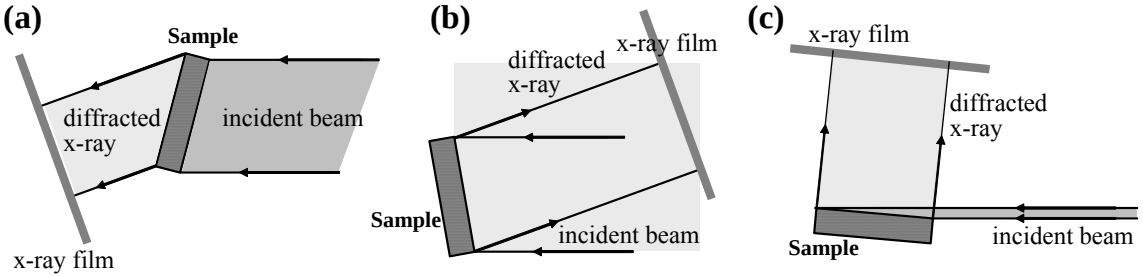

Figure 10. Schematics of transmission (a), back-reflection (b) and grazing-incidence reflection (c) geometries used in our studies.

Off-oriented *4H*-SiC substrates are usually used in epilayer growth because of the advantage of step-controlled growth and we are giving the detailed values of the structure factors for 8^{o} off-cut *4H*-SiC samples in the commonly used geometries. The schematics showing the geometries used in most of our studies are given in Figure 111.

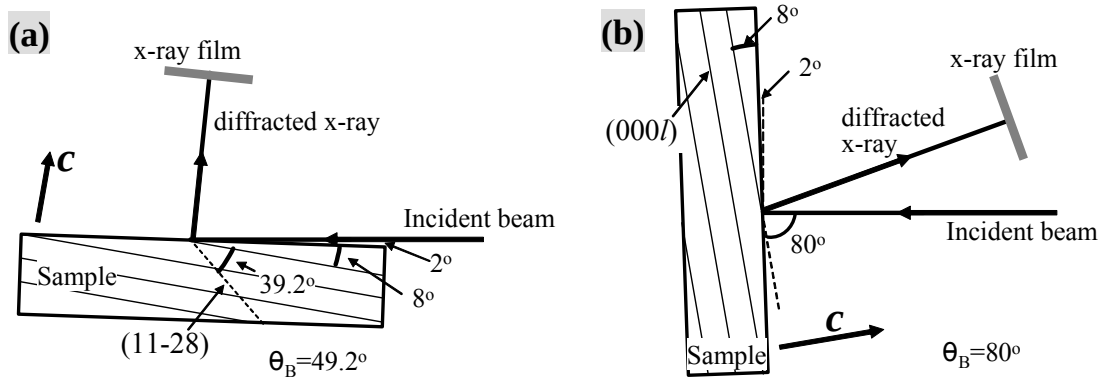

Figure 11. Schematics showing the geometries used in (11-28) grazing-incidence XRT (a) and back-reflection XRT (b) of an 8o off-cut SiC sample.

2.2. Molten Potassium Hydroxide Etching

Molten potassium hydroxide etching is an effective method to reveal the defects on the SiC crystal surface. It was carried out by soaking the specimens in liquid KOH at 600 ^{o}C for 10 min. The correspondence between etch pits and defects has been studied by Takahashi et al. [46] The etch pits patterns are usually recorded to comare with XRT as a complement.

3. Preliminary Results and Discussion

3.1. The Effect of Substrate Surface Scratches on CVD Grown Epilayer Quality

3.1.1. Outline

The influence of substrate surface scratches on the quality of CVD grown 4H-SiC homo-epitaxial layers has been studied using a combination of post-growth MSXT and KOH etching. MSXT observations suggest that the scratches on the substrate surface act as dislocation nucleation centers during the growth. TED-TED pairs, TED-BPD pairs, TSD-TSD pairs and Carrot defects are generated at scratches. Models are presented for the possible mechanisms for the nucleation of dislocations at scratches.

3.1.2. Introduction

Silicon Carbide (SiC) is a wide gap semiconductor material with excellent electronic and physical properties such as high electron draft velocity, high breakdown field and high thermal conductivity. These properties make SiC promising for certain extreme applications including high voltage, high power and high temperature devices.[11] However, the applications of these devices are hampered by the various defects in epilayers, which can degrade the performance of SiC devices significantly. Chemical vapor deposition (CVD) is the most widely used technique to grow epitaxial layers for SiC device fabrications.[47] Understanding the defect propagation/conversion and generation during CVD growth is therefore an important issue, and numerous studies have been reported.[27, 48, 49, 50] While the general picture of defect propagation/conversion from the substrate may be understood to a certain extent, the nucleation of defects near the interface between the substrate and epilayer has not received much attention. Surface scratches, residual from polishing, are generally accepted as dislocation nucleation sites during the epitaxial growth although no detailed mechanism for this process has been reported. In this paper, we present a study of defect nucleation at substrate surface scratches. We discuss the mechanism by which scratches become sources of dislocations and discuss its dependence on the angle between the scratch and the off-cut direction.

3.1.3. Experimental

Commercially available 4H-SiC wafers grown by the physical vapor transport (PVT) technique with an 8° off-cut angle toward the $[11\bar{2}0]$ direction were used as the substrates for chemical vapor deposition. After CVD growth, monochromatic synchrotron x-ray topographs were recorded from the epilayer using the (11-28) reflection. X-ray topographs were recorded in grazing incidence such that the penetration depth allowed for imaging of the whole epilayer thickness down to beyond the interface. The samples were etched in molten potassium hydroxide (KOH) at 600°C for 10 min. following the grazing x-ray topography. The etch patterns were recorded for further comparison with x-ray topographs.

3.1.4. Results and discussion

Figure 12(a) (c) (e) are $(11\bar{2}8)$ grazing-incidence monochromatic synchrotron x-ray topography (MSXT) images from the epilayer surface and Fig. 1(b) (d) (f) are the corresponding etch pit patterns. The $[1\bar{1}20]$ off-cut direction is vertical in Fig. 12. Some examples of the nucleation of dislocations along scratches can be clearly seen in Fig. 12 and it is observed that the orientation of the scratch with respect to the off-cut direction exerts influence over the process. When scratches were parallel to the off-cut direction (see Fig. 12(a)-(b)), they manifested themselves on the topographs as a single white band of contrast and on KOH etch patterns as a single, dense row of etch pits along the direction of the scratch. Magnified images show that this dense row consists of a high density of small hexagonal pits which are associated with threading edge dislocations (TEDs). [46] For scratches inclined to the off-cut direction (see Fig. 12(c)-(f)), X-ray topography reveals a similar single white band but with additional linear features attached which project along the off-cut direction. These linear features have been verified as basal plane dislocations (BPDs) and their measured lengths correspond to the thickness of the epilayer projected along the basal plane. KOH etching reveals a similar dense row of etch pits with a less dense row parallel to it at some distance which also corresponds to the projected thickness of the epilayer. The less dense row is confirmed to consist of oval shape pits which are associated with BPDs. [46] There are more linear features in Fig. 12(e) than that in Fig. 12(c) and a denser row of oval pits typifying the generally observed trend that the density of the BPDs associated with the scratch increases with the angle between the scratch direction and off-cut direction.

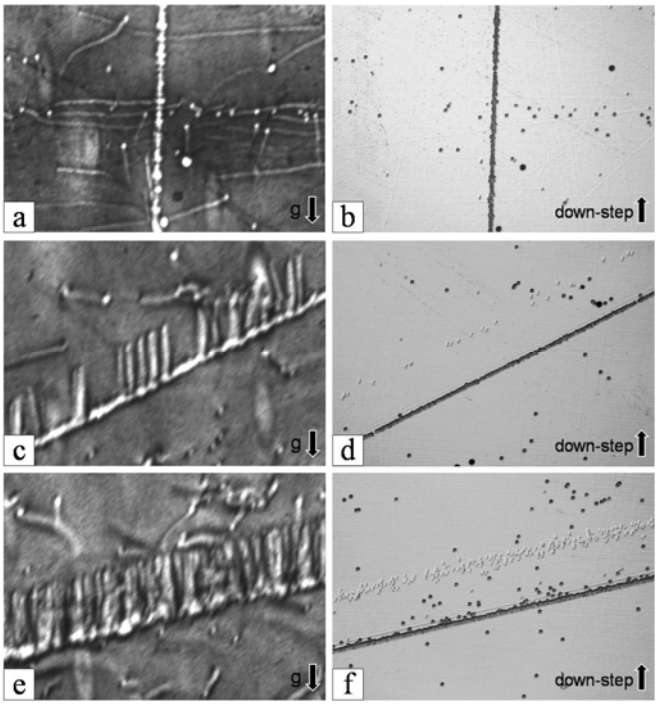

Figure 12. Synchrotron X-ray topographs ((a), (c) and (e)) and corresponding etch pit patterns ((b), (d) and (f)) recorded from epilayers grown on a scratched substrate surface. (a)-(b) show a scratch parallel to the off-cut direction while (c)-(f) show scratches inclined to the off-cut direction.

Figs. 13(a) and (b) shows enlarged topographic and etch pit images of one of the linear features from a similar region to Fig. 12(c). In Fig. 13(a), the linear feature appears as a diffuse band of white contrast separating two narrower dark bands all of which project along the off-cut direction, starting from the scratch and intersecting the epilayer surface. The bimodal dark contrast features exhibit a mutual shift along the line direction such that the left hand feature is slightly higher than the right hand one. This contrast is typical of a screw dislocation with the sense of the mutual shift reflecting the right-handed sense of the dislocation. [51] The etch pit at the intersection of this linear defect with the epilayer surface is an oval in shape (see Fig. 13(b)) corresponding to a BPD. From these two observations, it can be concluded that it is a BPD with a large right-handed screw component. Fig. 13(b) also reveals that the newly generated TEDs were nucleated in pairs. A distribution of six such pairs of closely spaced TED etch pits (marked with gray arrows) is shown in Fig. 13(b). While the TED pits in these pairs can just be resolved, the images of the TEDs comprising these pairs cannot be resolved in the X-ray topograph. In addition to paired TEDs, occasionally individual TED etch pits are observed which are paired with a single BPD etch pit (marked with black arrows) located at a distance along the off-cut direction corresponding to the thickness of the epilayer projected along the basal plane. These configurations are consistent with a row of TEDs propagating directly from the scratch to the epilayer surface (approximately along the epilayer surface normal) combined with occasional BPDs which propagate from the scratch to the epilayer surface on the basal plane.

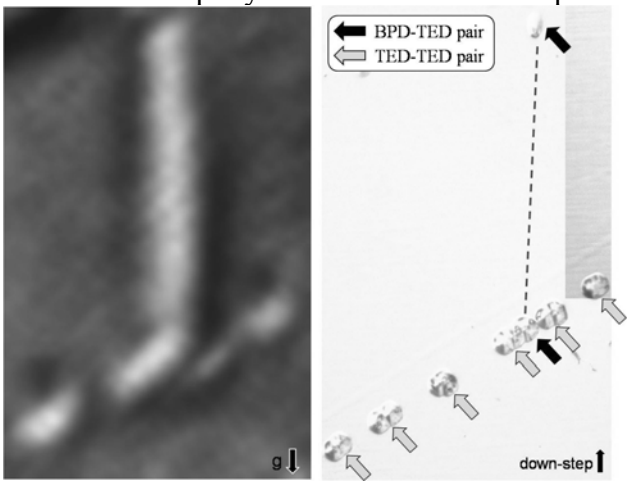

Figure 13. (a) Enlarged X-ray topograph recorded from a region similar to Fig. 12(c); (b) Corresponding etch pit pattern showing six pairs of TEDs (gray arrows) and a single paired TED and BPD (black arrows) which have propagated from the scratch to the epilayer surface.

SiC has been shown to demonstrate strong slip anisotropy in that the only slip systems activated under various loading conditions is the basal plane slip system. [52] It is therefore likely that deformation occurring at scratches during polishing would be confined to this system. Further, it is likely that such deformation would occur through the injection of half loops of BPD. Most of the deformation associated with the polishing process is likely to be removed during the Hydrogen etching carried out prior to CVD growth although some of the deformation associated with the deeper scratches might possibly persist as shown schematically in Fig. 14(a).

During CVD growth, the residual BPD half-loops associated with the deeper scratches can be replicated during growth. This replication involves conversion of the original deformation induced half-loops, at their points of surface intersection, into pairs of growth dislocations. The character of the growth dislocations produced during this conversion process is determined by the character of the two surface intersections of the BPD half loops which, in turn, is largely determined by the angle between the original scratch and the off-cut direction. Fig. 14 shows a scratch at a large angle to the off-cut direction. For the basal plane slip system with Burgers vector parallel to the off-cut direction, one side of the half loop would intersect the surface close to screw orientation while the other side would be close to edge orientation. It is well known that BPDs intersecting a growth surface close to screw orientation are likely to be replicated on the basal plane in contrast to edge oriented surface intersections which are likely to be converted to TEDs. [53] Thus, such half loops are likely to lead to the production of one BPD and one TED during CVD growth as shown in Fig. 14(b). On the other hand, for scratches parallel to the off-cut direction, both ends of the half loops will intersect the surface close to edge orientation and thus will replicate as TED pairs (see Figs. 12(a) and (b)). As the inclination between the scratch and the off-cut direction increases, so does the probability that at least one of the ends of the half-loop will have significant screw character and thus be expected to replicate during growth as a screw character BPD (as in Figs. 13(a) and (b)). In such cases, TED-BPD pairs are expected to be distributed amongst the TED-TED pairs. Further confirmation for our model is provided by the observation in Fig. 13(a) that the BPD in Fig. 13(a) exhibits bimodal contrast with mutual shift along the line direction which is typical of a screw character BPD. [51] Generally, cases where both ends of the half-loop propagate as TEDs dominate while those where one end propagated as a screw character BPD were less commonly observed. This is consistent with previous studies indicating a 70%-90% conversion rate of BPDs to TEDs.[54]

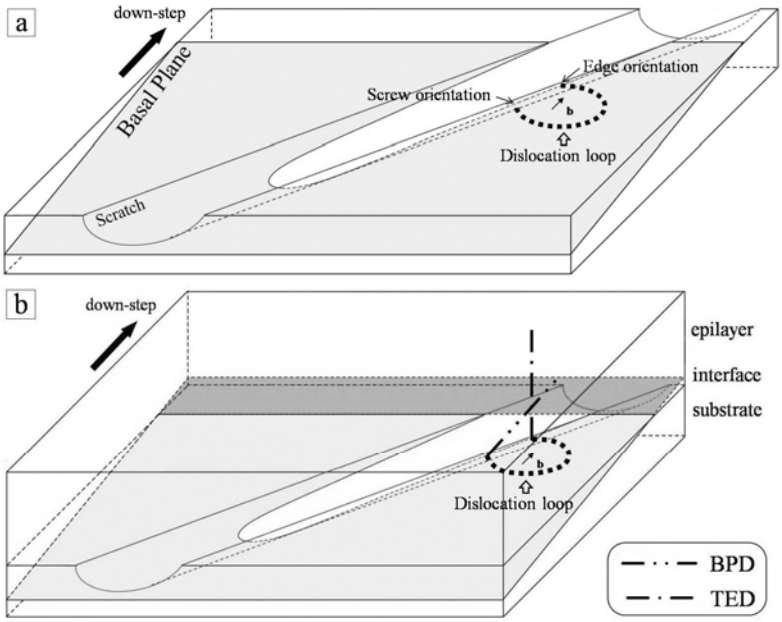

Figure 14. Schematic diagrams show (a) generation of dislocation loops near the substrate surface due to the scratch, and (b) Two possibilities for replication of the loop surface intersections during CVD epitaxial growth.

MSXT and KOH etching pattern of some other samples reveal that TSDs can also be nucleated along substrate surface scratches. There are two scratches visible in Figs. 15(a) and (b). On the topographs both of them have linear features attached to them which project along the off-cut direction. X-ray topography reveals the lower one as a single white band which is similar to the cases we discussed above. Compared with the etch pit pattern, it is clear that only TEDs and BPDs nucleated along it. But the upper one manifested itself on the topographs as a single but wider white band of contrast. The corresponding etch pit pattern confirmed that some other dislocations whose pits are bigger and deeper than TED etch pits were also nucleated along the scratch. Fig. 15(c) shows an enlarged area and it is observed that these dislocations appear as large hexagonal pits which correspond to elementary TSDs. [46]

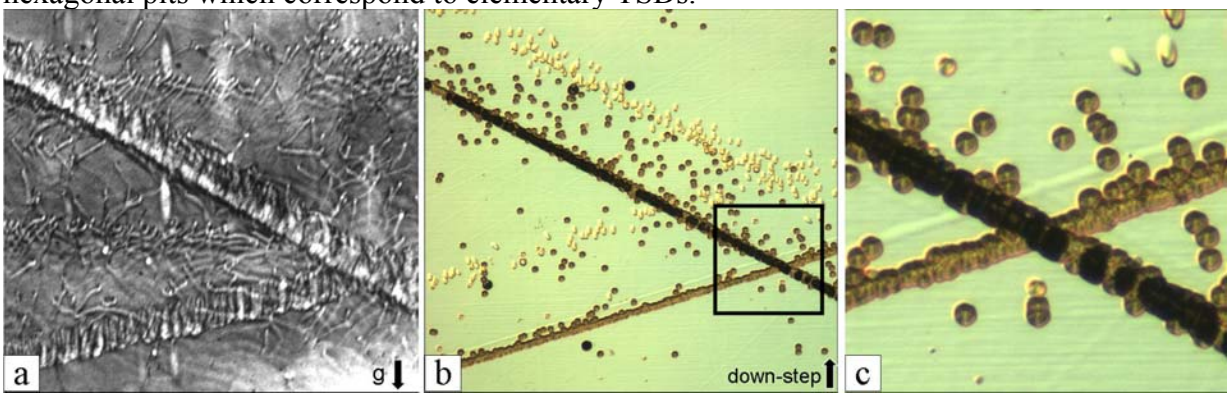

Figure 15. Synchrotron X-ray topographs (a) and corresponding etch pit patterns (b) recorded from epilayers grown on a scratched substrate surface. (c) Enlarged etch pit pattern from a region indicated in Fig. 15(b).

A nucleation mechanism for screw dislocations at inclusions has been previously proposed by our group. [22] Here we extend this approach to explain the observed nucleation of TSDs along scratches. As shown in Fig. 16, this model assumes that the scratch groove is not uniform but has a graded bottom. Atomic steps which approach these local surface indentations can collapse, as shown in Fig. 16, creating two screw dislocations of opposite sign which have Burgers vector magnitude equal to the magnitude of the step disregistry.

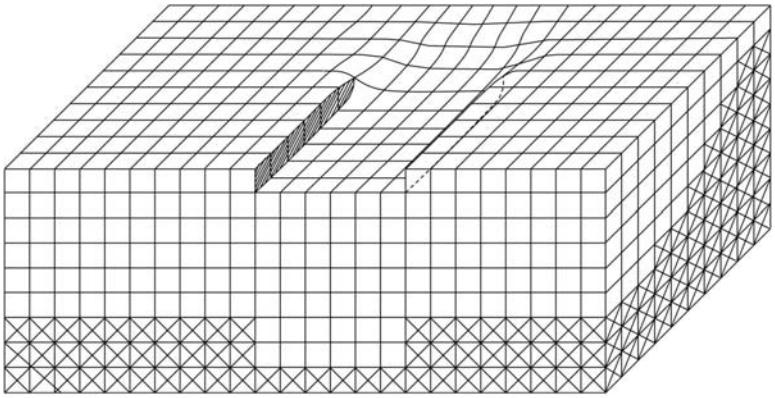

Figure 16. Schematic diagram illustrating the nucleation of a pair of opposite-sign screw dislocations during the process of scratch overgrow.

Fig. 17 shows an example of nucleation of TSDs along the scratch where the density of the nucleated TSDs is relatively low. It reveals clearly a distribution of five TSD pairs (indicated by pairs of arrows) which confirms our proposed mechanism. It is interesting that carrot defects are found to be associated with the nucleated TSDs for the two pairs in the upper region of Fig. 17. For each pair, a carrot defect is connected with one of the TSDs which is shifted from the position of the scratch groove. This is consistent with our previously proposed mechanism for the formation of carrot defects. [55] The updated and detailed nucleation mechanism for carrot defects at scratches still needs some further studies.

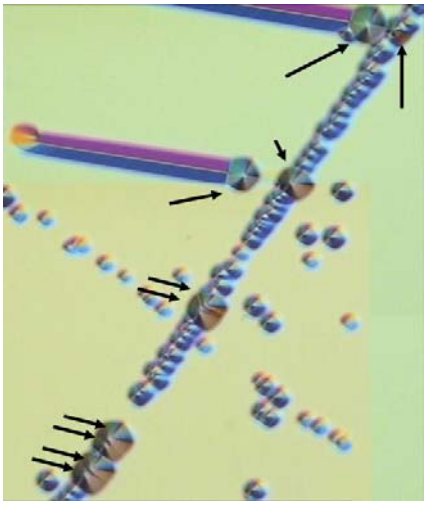

Figure 17. Etch pit pattern showing five pairs of TSDs and two of them are attached with carrot defects.

3.1.5. Conclusion

In summary, the influence of surface damage associated with scratches on the substrate surface has been investigated. We have demonstrated that various kinds of dislocations can be nucleated along the scratches which can propagate into the epilayers. Nucleation mechanisms are proposed although further studies will be needed to fully understand the processes. This latter work underlines the importance of good surface preparation prior to CVD growth.

3.2. The Nucleation Mechanism of Dislocation Half-Loop Arrays in 4H-SiC Homo-Epitaxial Layers

3.2.1. Outline

A model is presented for the formation mechanism of dislocation half loop arrays formed during the homo-epitaxial growth of 4H-SiC. The reorientation during glide of originally screw oriented threading segments of basal plane dislocation (BPD) endows them with significant edge component, rendering them susceptible to conversion into sessile threading edge dislocations (TEDs), which subsequently pin the motion of the BPD near the epitaxial surface. Continued glide during further growth enables parts of the mobile BPD to escape through the surface leaving arrays of half loops comprising two TEDs and a short BPD segment with significant edge component. The faulting behavior of the arrays under UV excitation is consistent with this model.

3.2.2. Introduction

Defect-related issues in silicon carbide (SiC) have posed significant barriers to the broader implementation of SiC-based devices. [56] A case in point is the behavior of basal plane dislocations (BPDs) in the epilayer regions of *p-i-n* devices operated under forward bias. The BPDs, which comprise pairs of Shockley partial dislocations separated by narrow ribbons of Shockley fault (~33nm wide in 4H-SiC), [31] are observed to further dissociate via the recombination enhanced dislocation glide (REDG) of Si-core partials causing expansion of the Shockley faults on the basal plane, a phenomenon which leads to lifetime limiting forward voltage drops. [12] BPDs in the epilayers largely result from the replication, during growth, of BPDs which intersect the surface of the off-cut SiC substrates, a process which can be mitigated by the conversion of the BPDs into threading edge dislocations (TEDs) [27] which are not susceptible to REDG. While various schemes have been developed to increase the conversion rate to nearly 100%, [54, 57, 58, 59] BPDs which intersect the surface in screw orientation are observed to persist, [53] and further, they are observed to nucleate half loop arrays via a mechanism which has, to date remained elusive. These HLAs provide new sources of BPDs which expand under forward bias. [27, 59, 60] In this letter we present a model for the formation of HLAs which successfully explains all of their observed features including their behavior during subsequent UV excitation.

3.2.3. Experimental

The 4H-SiC substrates used in this study were commercially available wafers sliced with an 8° off-cut angle towards the [11-20] direction from physical vapor transport (PVT) grown boules. The epitaxial layer is 100 μm thick and has n- doping of a few times $10^{14}/cm^3$. The paths of BPDs through the epitaxy were tracked using ultraviolet photoluminescence (UVPL) imaging, which is described elsewhere. [58, 61]

3.2.4. Results and discussion

A HLA configuration, typical of those reported earlier, [59] recorded using UVPL imaging in plan-view from a Si-face epilayer, is shown in Fig. 18(a). According to current understanding, the screw oriented BPD in the epilayer (marked BC) undergoes sideways glide under the action of lattice mismatch stress [62] leaving a trailing interfacial dislocation (ID) at or near the substrate/epilayer interface (marked AB) and trails of dislocation configurations known as half loop arrays (HLAs; the array of dots along DC) in the epilayers. [60, 62, 63, 64, 65] The motion of the ID towards the interface has evidently been impeded forcing it to settle at some 40μm above the interface. This particular image was chosen since if the dislocation were in fact at the interface it would be invisible on the UVPL image because its luminescence would be quenched by the adjacent heavily doped substrate. Previous work has shown that there are pairs of closely-spaced TED surface intersections associated with each of the dots in the HLA, and based on the behavior of the HLAs in *p-i-n* diodes under forward bias these are connected by a short BPD segment to form a half loop. [27, 60] When the as-grown sample is subsequently subjected to extended UV exposure, electron-hole recombination causes the BPD segment at each of the white dots in the HLA in Fig. 18(a) to expand in the form of rhombic shaped Shockley faults as shown in Fig. 18(b) and schematically in Fig. 18(c). The two brighter segments bounding each rhombic shape, which expand in opposite directions, are mobile Si-core partials leaving the two fainter segments which are the immobile C-core partials, as shown in Figure 18(b). Both types of partials have been shown to have 30° character. [34] As expansion continues further, the partials emanating from adjacent HLA basal segments merge and annihilate indicating that they are all on the exact same basal plane (see Fig. 18(d)). The expansion of the faults continues until they span the epilayer. [34] In Fig. 18(b), the stacking fault expansion above the original HLA eventually reaches the top of the epitaxy and the stacking fault expansion below the HLA reaches the substrate. The depths of the BPD segments of the HLA and of the ID are determined by the distance the stacking fault expands before reaching the epitaxial surface. It should be noted that, during UV exposure, the ID does not experience stacking fault expansion along most of its length except at short segments (e.g. those indicated by arrow tips) where pinning causes its line direction to deviate sufficiently from [1-100] to endow it with a significant screw component.

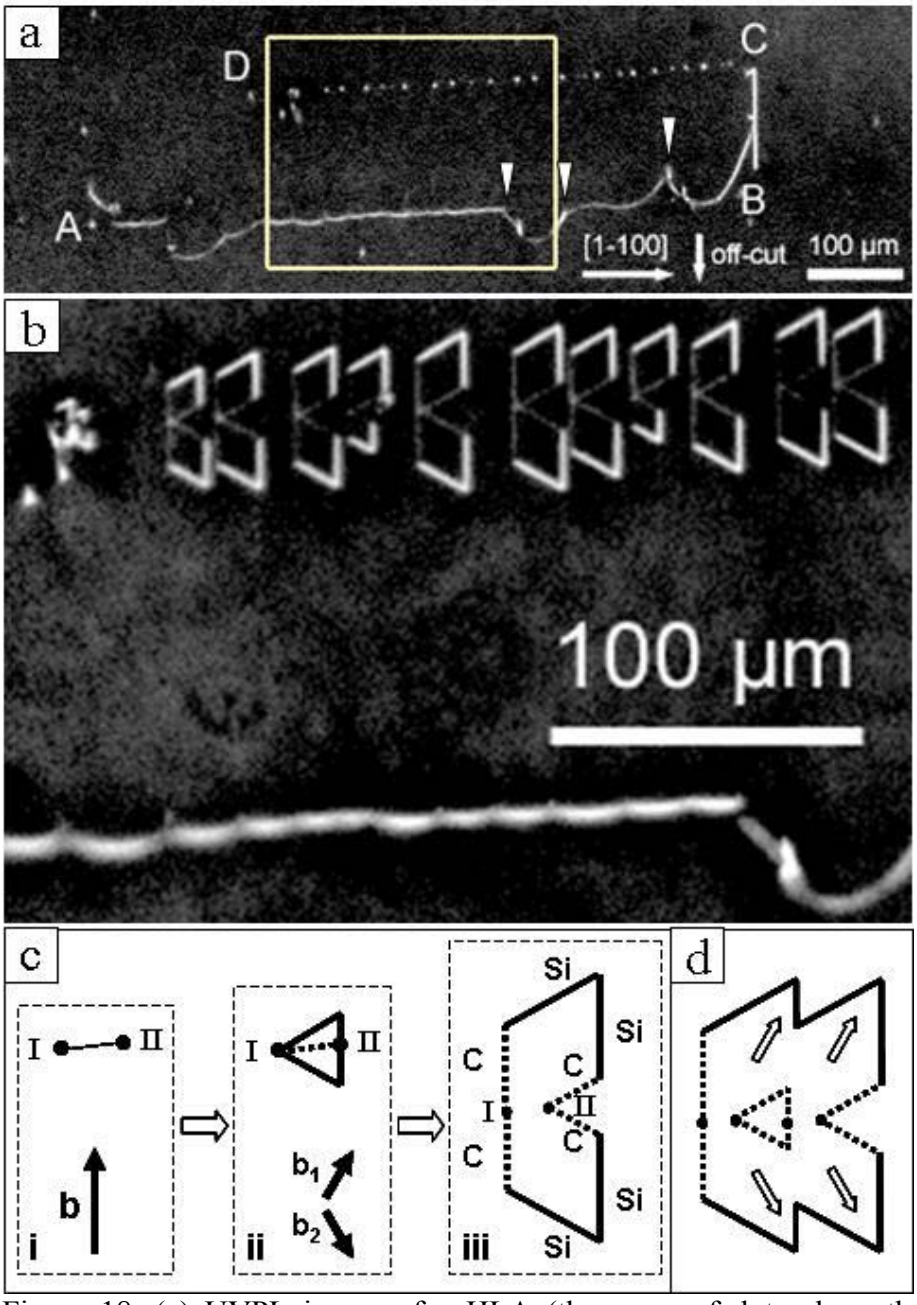

Figure 18. (a) UVPL image of a HLA (the array of dots along the line DC) before extended UV exposure. The HLA is connected to the mobile threading segment of the BPD at C. The interfacial segment of BPD is along AB; (b) Magnified view of boxed area in Fig. 1(a) after extended UV exposure. (c) Schematic diagram showing the evolution of the rhombic shaped faults during dissociation. In (i), the initial BPD segment runs between I and II. In (ii), this dissociates in the form two inclined and two vertical segments of mobile, Si-core, 30° partial. In (iii), further expansion requires the creation of two inclined and two vertical segments of less mobile, C-core, 30° partial. (d) At a later stage (not shown), as the Si-core partials from one element in the HLA meet the C-core partials from the adjacent element, annihilation occurs. This indicates that all of the partials are on the exact same basal plane.

For an undissociated BPD, the magnitude of the 1/3<11-20> Burgers vector is twice the *d*-spacing of the (11-20) planes so that dislocations close to edge orientation are expected to have cores comprising two extra half planes as shown in Fig. 19(a) (as was originally established for HCP materials).[66] Upon dissociation, partials of the same sign are expected, with either Si or C-core depending on the sign of the original dislocation, separated by a Shockley fault as shown in Figs. 19(b) and (c). Likewise, if dislocations with significant screw components dissociate, opposite sign partials are expected as shown in Figs. 19(d) and (e). Since the BPD segments associated with the HLA are observed, under UV excitation, to expand in opposite directions with same sign Si-core partials (leaving trailing C-core partials; Fig. 18(b)), the BPD segments at the bottom of the half loops have large edge component as shown in Fig. 19(b). Meanwhile, most of the length of the ID does not expand in either direction so that is likely to have large C-core edge character, as shown in Fig. 19(c). This enables the Burgers vector of the large edge component ID and the BPD segments of the HLA to be identified as 1/3[11-20] and 1/3[-1-120], both of which project parallel to the off-cut direction. This is consistent with the fact that the ID and the BPD segments of the HLA originate from the same gliding BPD but have nearly opposite line directions.

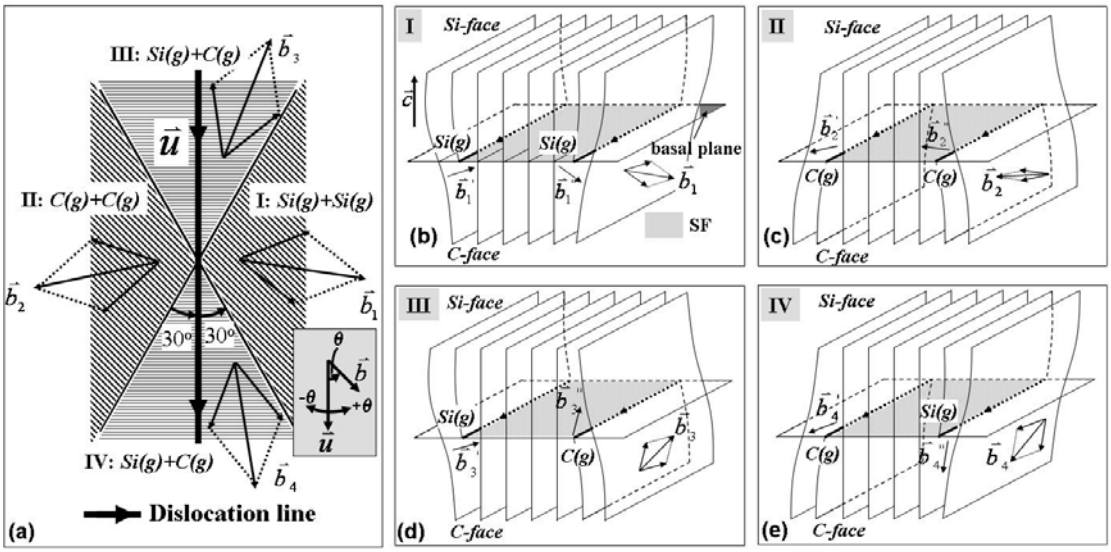

Figure 19. Schematics showing Shockley partial dislocations of different core structures dissociated from a perfect BPD. (a) Partial dislocation core structure for various angles θ between the Burgers vector, **b**, and line direction, **u**, of the perfect BPD, defining regions I-IV; (b) Region I: $30^o<\theta<150^o$, the BPD is dissociated into two Si-core partials; (c) $210^o<\theta<330^o$, the BPD is dissociated into two C-core partials; (d) $-30^o<\theta<30^o$, one Si-core and one C-core; (e) $150^o<\theta<210^o$, one Si-core and one C-core. θ is defined in the inset of (a).

Regarding the HLA formation mechanism, Fig. 3(a) shows a screw-type BPD with Burgers vector 1/3[11-20] intersecting the surface of the substrate which is expected to be replicated during epitaxy in contrast to those with significant edge components which are likely to be converted into TEDs. [53] As soon as the epilayer exceeds critical thickness, as per the predictions of Matthews and Blakeslee, [67] the threading segment of the screw oriented BPD will be forced to glide sideways leaving a trailing interfacial

segment in its wake at or near the substrate/epilayer interface. During this glide process, the mobile threading segment adopts more edge character near the growth surface (see Fig. 20(b)) rendering it susceptible to conversion to a TED during continued growth. Slip in SiC is confined to the basal plane, [52] so that the sessile TED segment pins the surface intersection of the mobile BPD segment. During further growth, the TED segment is replicated while the mobile basal segment of dislocation pivots about the pinning point as shown in Fig. 20(c). At this juncture, part of the mobile BPD segment can escape through the epilayer surface (creating a surface step of magnitude equal to the Burgers vector), as shown in Fig. 20(d) leaving two further BPD surface intersections which, since they are not in screw orientation, are susceptible to conversion to TEDs. Upon conversion, one of these TEDs is connected via a short BPD segment to the TED segment created in Fig. 20(b), thus creating a half loop comprising two TEDs and a connecting BPD. The other TED again acts as a pinning point for the still mobile segment of threading BPD, as shown in Fig. 20(e), as the process repeats during continued growth as the TED segments further replicate and the threading BPD segment continues to glide. The net result of this process is an array of half loops with short, large edge component BPD segments, all deposited on the exact same basal plane. The direction of the array is nearly perpendicular to the off-cut direction as summarized in Fig. 20(f) and shown in Fig. 18(a). The value of this angle depends on the competition between the growth rate and the rate of sideways glide of the threading BPD segment. Note that the short BPD segments are not expected to glide under the mismatch stress since the force required for such a short segment pinned at both ends is much larger than for the longer threading segment. [45] This configuration is consistent with the observed expansion of the HLA BPD segments in opposite directions and the annihilation of opposite sign partials which merge from adjacent HLA elements.

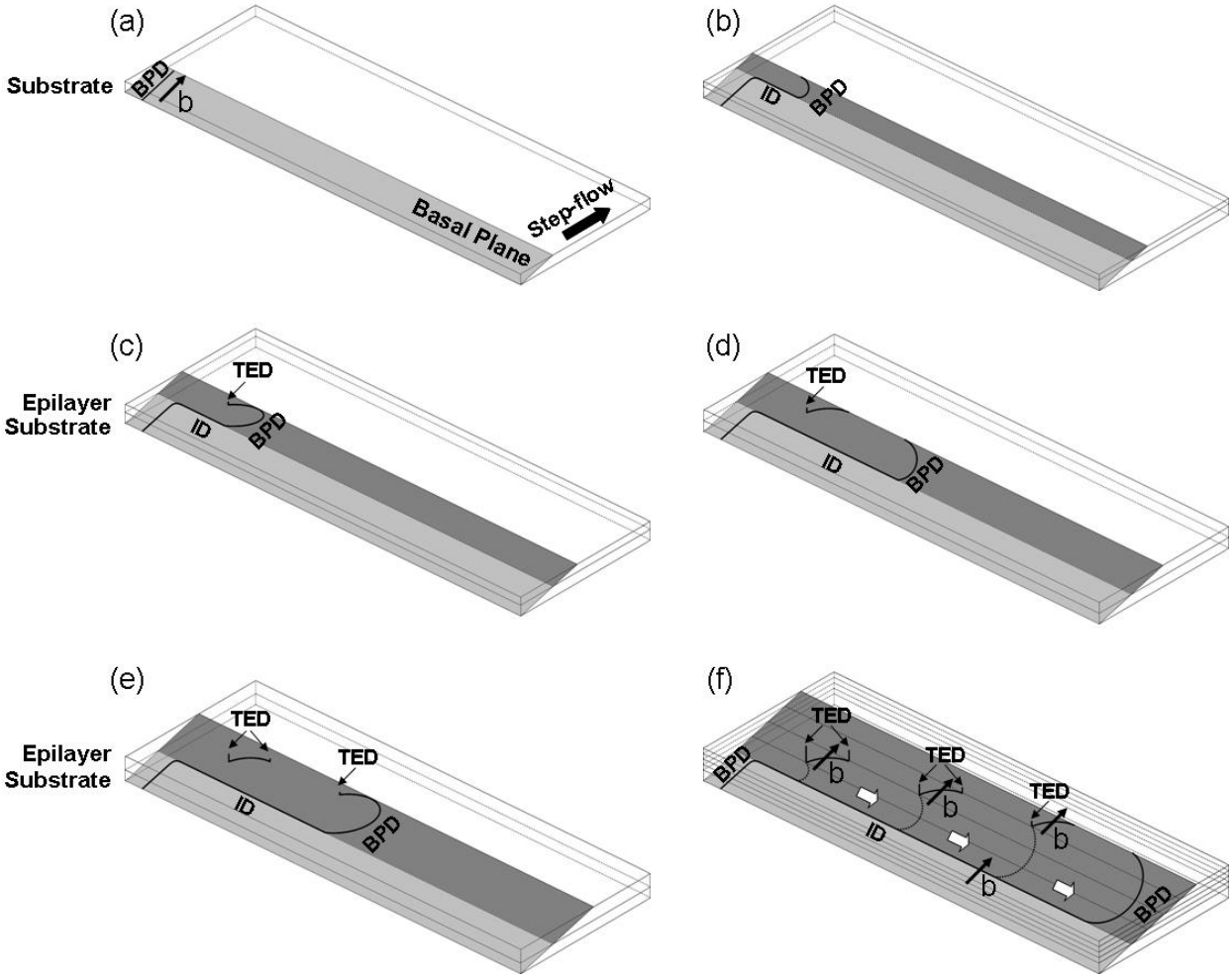

Figure 20. Schematic diagram showing the formation mechanism of a HLA. (a) – (e) sequential stages in the process; (f) Summary of process. The lighter shaded planes in (a)-(f) indicate the basal plane on which the BPD lies in the substrate, while the darker one lies in the epilayer. See text for details of mechanism.

3.2.5. Conclusion

In conclusion, a model has been presented for the formation mechanism of dislocation HLAs formed along with interfacial dislocations during the sideways glide of threading segments of screw oriented BPDs during the epitaxial growth of 4H-SiC. During glide, the surface intersections of the screw oriented BPDs adopt more edge character making them susceptible to conversion into sessile TEDs, which subsequently pin the motion of the BPD. Continued glide during further growth enables part of the mobile BPD to escape through the surface leaving two additional large edge component surface intersections which can again be converted into sessile TEDs. The process repeats leaving arrays of half loops comprising two TEDs and a short BPD segment with significant edge component. The faulting of the arrays under UV excitation and the lack of faulting of the associated interfacial dislocation is consistent with this model.

3.3. Strain/stress Mapping Analysis

3.1.1. Outline

Synchrotron white beam x-ray reticulography has been used to quantitatively map the residual stress/strain in SiC wafers. The basic principle of our study is that there exists a relationship between the stress state in a crystal and the local lattice plane orientation and that this relationship can be exploited in order to determine the full strain tensor as a function of position inside the crystal. The theoretical background involved in stress mapping using synchrotron white beam x-ray reticulography is introduced based on the change of the normal to a lattice plane due to the distortion associated with the residual strain. The stress in a region of a commercial 4*H* silicon carbide wafer has been studied using this technique and the results are discussed. This technique can in principle be used in any single crystal material.

3.1.2. Introduction

Silicon carbide (SiC) is well known as a potential semiconductor material for applications under extreme circumstances due to its outstanding properties such as high thermal conductivity, high breakdown voltage and high saturated electron drift velocity. Accurate measurement of the residual stress/strain in as-grown SiC crystals is of great interest because measured values can allow validation of the thermal stress calculations used to design optimal crystal growth parameters. This is of particular importance in SiC since thermal stresses lead to the activation of basal plane slip systems resulting in significant densities of basal plane dislocations which are implicated in the forward voltage drop under forward bias in pin diodes. Other techniques that can be used to measure stress distributions in SiC crystals include high-resolution x-ray diffraction and Raman spectroscopy. However, mapping the full strain/stress tensor using these techniques can be extremely time-consuming. Here we identify a technique which can be used to map the complete strain/stress state of a large-area SiC wafer in a fast, effective and accurate way. This technique is based on the application of the ray-tracing principle to x-ray reticulography. [68]

3.1.3. Experimental

A 3 in. 4H-SiC wafer that has been polished with diamond paste as small as 0.5 μm was studied. The measurement process and results on a 20 mm x 27 mm area are shown in this paper. This is the typical area that is choosed for the best efficiency and accuracy of the measuring process. It is easy and quick to duplicate the measurement on other areas and piece the results together in order to get the stress mapping of the whole wafer.

A fine scale x-ray absorbing mesh with periodicity of 1 mm placed on the x-ray exit surface of the sample splits the diffracted beams into an array of microbeams. The imaging was carried out at the Stony Brook Synchrotron Topography Station (Beamline X-19C) at Brookhaven National Laboratory using Agfa Structurix D3-SC film at a specimen-film distance of 10 - 15 cm for transmission geometry.

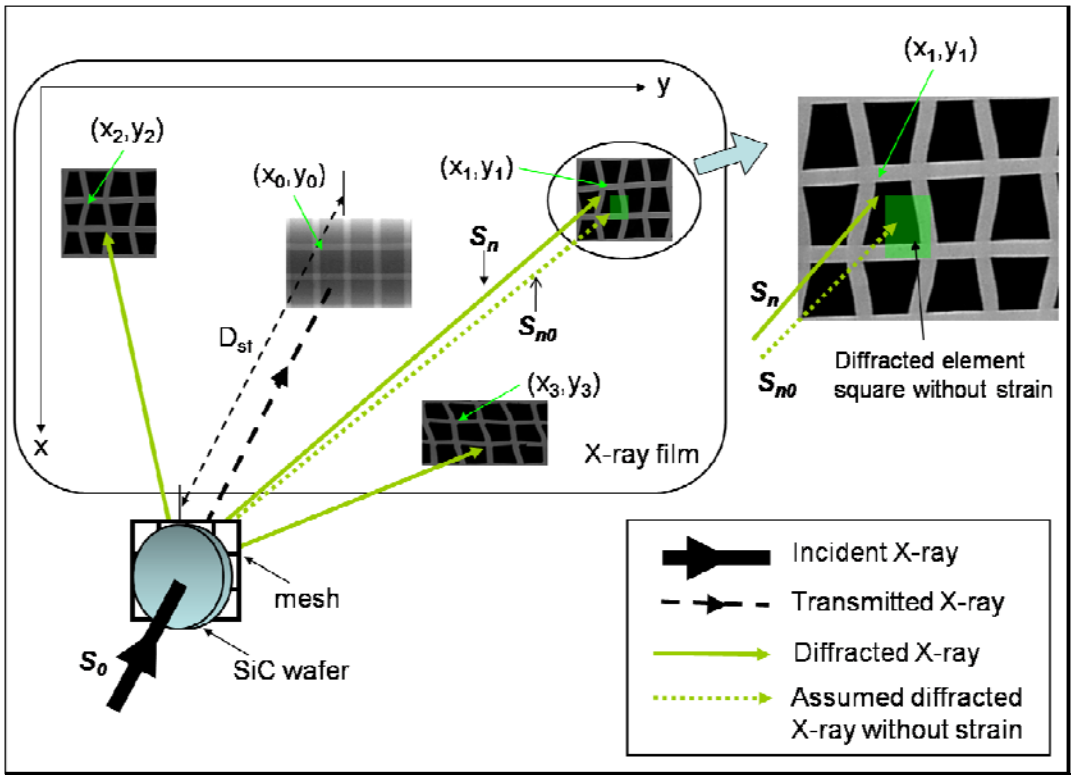

Figure 21. Schematic diagram showing the geometry used in the reticulography. (x_0, y_0), (x_1, y_1), (x_2, y_2) and (x_3, y_3) are the coordinates of the spots on the radiograph and three diffracted images. They are from the same location on the crystal surface.

Fig. 21 is a schematic representation reticulography experiment. In a Cartesian coordinate system, the *x* axis is selected parallel to [11-20], and the *y* axis is oriented along [1-100]. $(x_0, y_0), (x_1, y_1), (x_2, y_2)$ and (x_3, y_3) are the coordinates of the image of the point of interest in the crystal on the radiograph and three diffraction images. Since the mesh is right on the crystal surface, these four points actually correspond to the same position of the crystal. $\boldsymbol{S_0}$ is the unit vector of the incident beam. $\boldsymbol{S_n}$ is the vector of the diffracted beam and $\boldsymbol{S_{n0}}$ is the assumed vector of the diffracted beam if no strain exists in the SiC wafer.

3.1.4. Date processing, results and discussion

When the crystal is subjected to a displacement field, the original plane normal $\vec{n}^0$ for a given set of planes is modified to $\vec{n}$, according to the following equation

$$\vec{n}(x,y,z) = \vec{n}^0(x,y,z) - \nabla\left[\vec{n}^0(x,y,z)\cdot\vec{u}(x,y,z)\right] \quad (1)$$

where $\vec{n}^0(x,y,z)$ is the plane normal at (*x, y, z*) before distortion, $\vec{n}(x,y,z)$ is the plane normal at (*x, y, z*) after distortion and $\vec{u}(x,y,z)$ is the displacement vector at (*x, y, z*). Fig. 22 gives the physical meaning of the equation (1). $\nabla\left[\vec{n}^0(x,y,z)\cdot\vec{u}(x,y,z)\right]$ is the vector

point toward the direction of the greatest rate of increase of $\vec{n}^0(x,y,z)\cdot\vec{u}(x,y,z)$ and $\vec{n}^0(x,y,z)-\nabla\left[\vec{n}^0(x,y,z)\cdot\vec{u}(x,y,z)\right]$ is the vector (not unit vector) perpendicular to the plane after deformation.

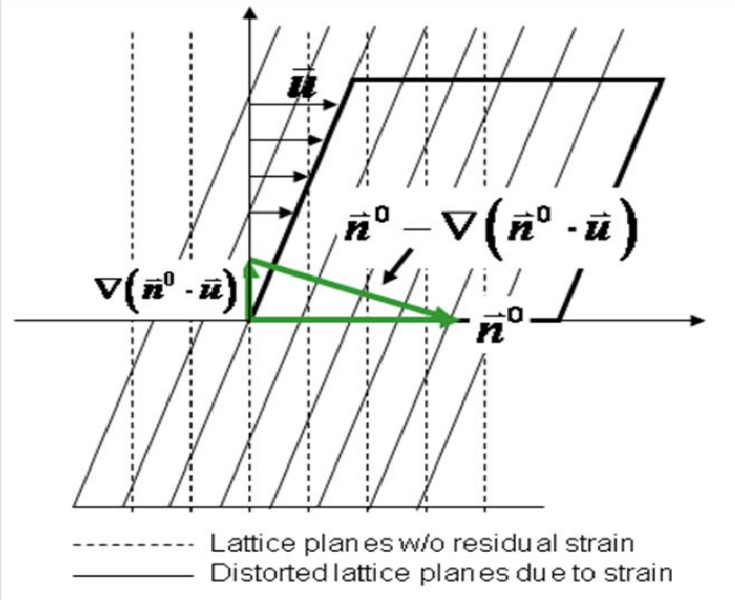

Figure 22. Schematics showing the physical meaning of the equation (1). Dotted lines are lattice planes before distortion. Solid lines denotes lattice planes after distortion. $\vec{n}^0$ is the plane normal before distortion.

Note that the vector calculation in equation (1) must be carried out in the Cartesian coordinate system so that if the crystal structure is non-cubic, the crystal lattice vectors must first be expressed referred to such a Cartesian system. Calculate $\vec{n}(x,y,z)$ using equation (1), and separate it into three components.

$$\begin{cases} n_x = n_x^0 - \left(n_x^0 \dfrac{\partial u_x}{\partial x} + n_y^0 \dfrac{\partial u_y}{\partial x} + n_z^0 \dfrac{\partial u_z}{\partial x} \right) \\ n_y = n_y^0 - \left(n_x^0 \dfrac{\partial u_x}{\partial y} + n_y^0 \dfrac{\partial u_y}{\partial y} + n_z^0 \dfrac{\partial u_z}{\partial y} \right) \\ n_z = n_z^0 - \left(n_x^0 \dfrac{\partial u_x}{\partial z} + n_y^0 \dfrac{\partial u_y}{\partial z} + n_z^0 \dfrac{\partial u_z}{\partial z} \right) \end{cases}. \quad (2)$$

In equation (2), $\frac{\partial u_x}{\partial x}, \frac{\partial u_x}{\partial y}, \frac{\partial u_x}{\partial z}, \frac{\partial u_y}{\partial x}, \frac{\partial u_y}{\partial y}, \frac{\partial u_y}{\partial z}, \frac{\partial u_z}{\partial x}, \frac{\partial u_z}{\partial y}, \frac{\partial u_z}{\partial z}$ are nine unknown tensor components. Three groups of equations like equation (2), totally nine equations, can be generated if measurements are made on three topographic reflection spots thus determining the components of three modified plane normal: $n_{1x}, n_{1y}, n_{1z}, n_{2x}, n_{2y}, n_{2z}, n_{3x}, n_{3y}, n_{3z}$. The nine unknowns can be calculated by numerically determining the solutions of these nine equations. This process was

computer-assisted by Mathematica v5.1. Then the strains can be calculated by its definition

$$\varepsilon_{ij} = \frac{1}{2}\left(\frac{\partial u_i}{\partial x_j} + \frac{\partial u_j}{\partial x_i}\right). \tag{3}$$

The corresponding stress component can be subsequently calculated, provided the shear modulus or Young's modulus.

After the reticulographic image is recorded, mapping of the strain (and thereby the stress) is carried out as follows. First, select the radiograph and three diffraction spots as shown in Fig. 21. Extract the coordinates of the correlated corners from the x-ray film. An automatic image recognition program was used here to assist the extraction process. Second, calculate the plane normal before distortion, $\vec{n}^0$ $\left(\vec{n}^0 = \vec{S}_{n0} - \vec{S}_0\right)$. This can be obtained by selecting a minimum stress point in the crystal. Third, calculate the plane normal after distortion, $\vec{n}$. This can be obtained by measuring the coordinates of each corner point and specimen-to-film distance. The second and third steps were realized by Mathematica software and the obtained $\vec{n}^0$ and $\vec{n}$ will be plugged into the previously discussed equation to calculate the nine unknown tensor components.

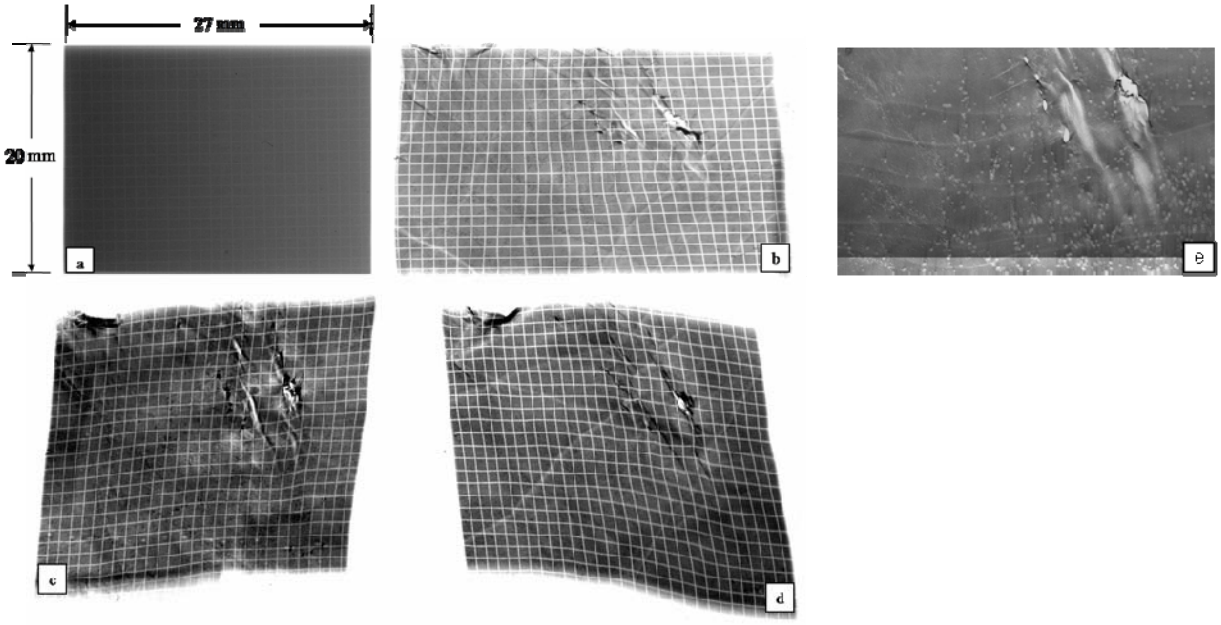

Figure 23. Transmitted radiograph (a), three diffracted images [(b), (c) and (d)] and SWBXT image (e) from the same crystal area.

Fig. 23 shows a transmitted radiograph, three corresponding diffracted images and Synchrotron White Beam X-ray Topography (SWBXT) image. The transmitted radiograph in Figure 3(a) is undistorted while the diffracted images in Figs. 23(b) – (d) are distorted. The diffracted images are distorted in different ways: Fig. 23(b) is stretched horizontally while Figs. 23(c) and (d) are skewed (also one is skewed in a different way from the other). These three diffracted images have been used in our calculation. In the diffracted images [(b) – (d)], a highly distorted region is visible near the upper right

corner, which is due to low angle grain boundaries (see Fig. 23(e)), indicating extremely high strain near this region. Nearly all the squares in the diffracted images are distorted. Such distortion contains not only the qualitative but also quantitative information regarding the residual strain.

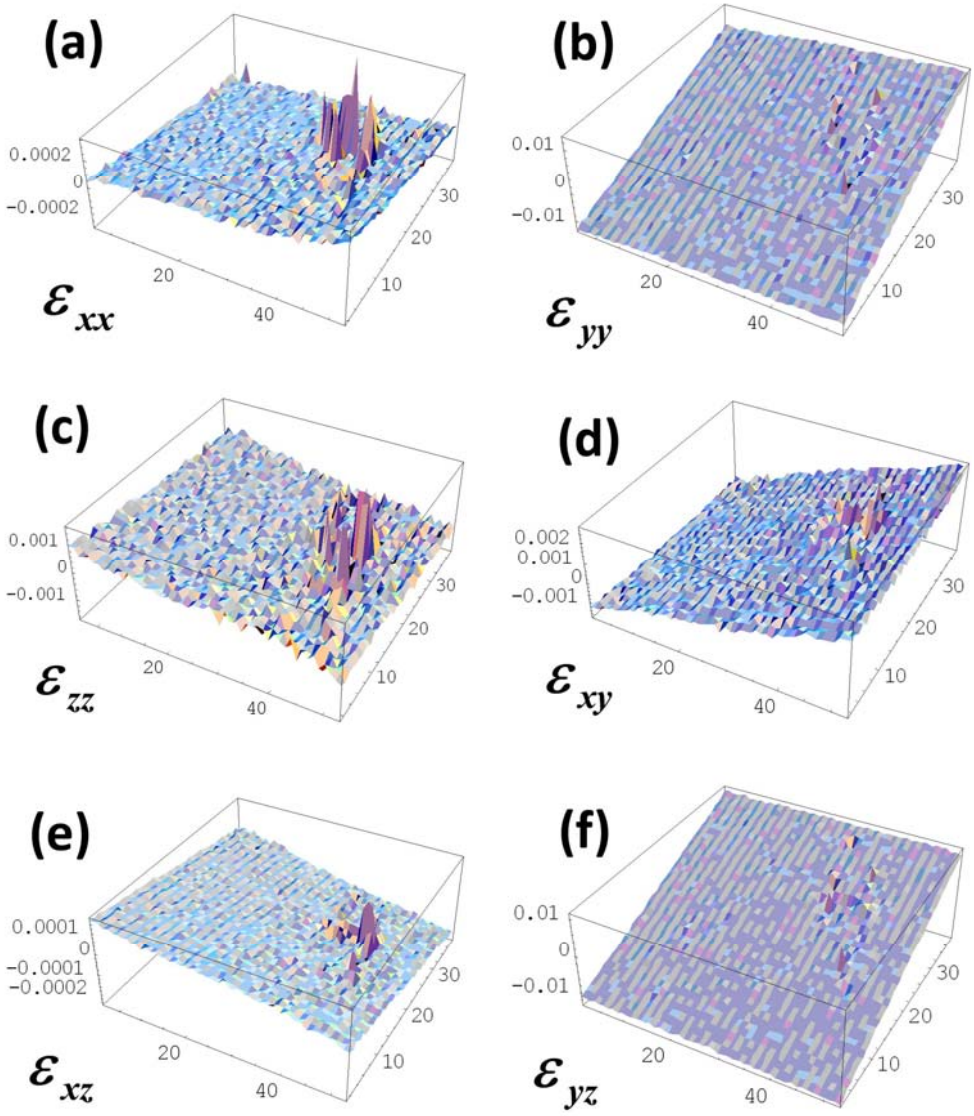

Figure 24. Strain mapping of a 20 mm x 27 mm region in a 3-inch SiC wafer. (a) – (f) are 3D mapping of the six strain components εxx, εyy, εzz, εxy, εxz and εyz, respectively.

Fig. 24 gives the 3D mapping of all the six strain components ε_{xx}, ε_{yy}, ε_{zz}, ε_{xy}, ε_{xz} and ε_{yz}. Each strain component is larger near low angle grain boundaries than that away from them. The residual strain in the wafer is very complicate and it may change from compressive strain to tensile strain [e.g., in (a) – (c)], or it may change its sign from one region to the other. Further confirmation and data processing is under way to improve the accuracy and resolution of the results.

3.1.5. Conclusion

Synchrotron White Beam X-ray Reticulography (SWBXR) has been demonstrated to be a fast, effective and accurate method to map the strain/stress state in SiC wafer. With the assistance of specially written image recognition software and Mathematica programming, the strain/stress data can be accurately and rapidly calculated and mapped. This method is especially convenient to apply to the mapping of stress over large crystal areas. This technique is broadly applicable to stress measurement in any single crystal.

4. Conclusions

Dislocation structures in SiC bulk crystals and epilayers have been studied using synchrotron x-ray topography as well as other characterization techniques.

I) The effect of substrate surface scratches on the quality of chemical vapor deposition (CVD) grown 4H-SiC homo-epitaxial layers has been studied using (Monochromatic Synchrotron X-ray Topography) MSXT and KOH etching techniques. The experimental results suggest that the scratches on the substrate surface act as a dislocation nucleation center during the growth. Various kinds of dislocations were observed to nucleate at the scratch, including TED-TED pairs, TED-BPD pairs, pairs of opposite sign screw dislocations and carrot defects. The models are presented for possible mechanisms of dislocation nucleation at the scratch. Further studies show that such effect and mechanism can also be applied to the physical vapor transpor (PVT) growth of bulk SiC crystals.

II) The formation mechanism of the dislocation half loop arrays (HLAs) in 4H-SiC homo-epitaxial layers has been investigated. The HLAs have been studied using a combination of MSXT and Ultraviolet Photoluminescence (UVPL). A model is presented for the formation mechanism of dislocation HLAs formed during the epitaxial growth. The reorientation during glide of the formerly screw character surface intersections of threading segments of BPD render them susceptible to conversion into sessile TED which subsequently pin the motion of the BPD. Continued glide during further growth enables parts of the mobile BPD to escape through the surface leaving arrays of half loops comprising two TEDs and a short BPD segment with significant edge component. The behavior of the arrays under UV excitation is consistent with this model.

III) A strain/stress mapping technique has been invented, based on ray-tracing principle. Synchrotron white beam x-ray reticulography has been used to quantitatively map the residual strain/stress in SiC wafers. The basic principle of our study is that there exists a relationship between the stress state in a crystal and the local lattice plane orientation and that this relationship can be exploited in order to determine the full strain tensor as a function of position inside the crystal. The stress in a region of a commercial 4H-SiC wafer has been studied using this technique and the results are discussed.

5. Future work

The nucleation mechanisms of the various types of dislocation in SiC still remain obscure. For example, no adequate explanation exists for the nucleation of individual TSDs, although opposite-sign screw or micropipe pairs can be nucleated at inclusions. Frank partial dislocations, which are associated with extra atomic half planes, are expected to play critical roles in the nucleation of micropipes and closed-core threading screw dislocations. TEDs, which exist at densities which can be one-order of magnitude higher than elementary threading screw dislocations in silicon carbide, have not yet been afforded enough attention. The nucleation mechanism of individual TEDs is still unknown. Although some of the threading edge dislocations could be converted from the basal plane dislocations during epitaxial growth, most of them are inherited from the substrates. It is therefore of great importance to study the nucleation of TSDs and TEDs in depth.

Epitaxy is the basis for device fabrication and many epilayer defects are still not fully understood. Our preliminary results reveal the nucleation mechanism of dislocation half loop arrays and various dislocations at scratches. However, the TSD pairs and carrot defects generated at scratches need to be further investigated. Previous researches in our group indicated that off-cut angle, growth rate and et al. have fundamental influences on generation/propagation/conversion of various dislocations in step-controlled epi-growth, such as that the closed-core threading screw dislocations can be converted into Frank partial dislocations during chemical vapor deposition on vicinal substrates. This provides a potential way to significantly reduce the density of various dislocations. Detailed studies on the mechanisms and growth parameters controlling the process will be focused on.

The dislocations in SiC devices will directly affect the electrical properties of devices, and their correlations with the device performance are of great interest. Although numerous works have been done on several dislocations, the influence of TEDs on device performance has not been reported. In additoni, the fully conversion of BPDs into TEDs in the device has not yet been achieved. Therefore, it is of great importance to study the structures and properties of dislocations in the devices and clarify their correlations with the device performance.

Reference

[1] L. S. Ramsdell, American Mineralogist **32**, 64 (1947)
[2] W. F. Knippenberg, Philips Res. Rept. **18**, 161 (1963)
[3] F. C. Frank, Phil. Mag. **42,** 1014 (1951)
[4] H. Jagodzinski, Acta Cryst. **7,** 300 (1954)
[5] G. Augustine, H. M. Hobgood, V. Balakrishna et al., Phys. Stat. Sol. (b) **202**, 137 (1997)
[6] Yu.M. Tairov and V.F. Tsvetkov, *J. Crystal Growth* **43,** 209 (1978)
[7] D. Chaussende, P. J. Wellmann, and M. Pons, J. Phys. D: Appl. Phys. **40**, 6150 (2007)
[8] R. W. Olesinski and G. J. Abbaschian, Bull. Alloy Phase Diagrams **5**, 486 (1984)
[9] K. Koga, Y. Fujikawa, Y. Ueda and T. Yamaguchi, Springer Proc. Phys. **71**, 96 (1992)
[10] P. G. Neudeck and J. A. Powell, IEEE Electron. Device Letters **15**, 63 (1994)
[11] P. G. Neudeck, W. Huang and M. Dudley, Solid-State Electronics **42**, 2157 (1998)
[12] H. Lendenmann, F. Dahlquist, N. Johansson, R. Soderholm, P. A. Nilsson, J. P. Bergman and P. Skytt, Mater. Sci. Forum **353-356**, 727 (2001)
[13] W. M. Vetter and M. Dudley, J. Appl. Phys. **96**, 348 (2004)
[14] M. Skowronski, in "Wide Energy Bnadgap Electronic Devices", Editors: F. Ren and J.C. Zolper, World Scientific Publishing Company, 2004, pp. 261
[15] E. K. Sanchez, J. Q. Liu, M. D. Graef, M. Skowronski, W. M. Vetter and M. Dudley, J. Appl. Phys. **91**, 1143 (2002)
[16] M. Dudley, S. Wang, W. Huang, C.H. Carter Jr., V.F. Tsvetkov and C. Fazi, J. Phys. D: Appl. Phys. **28**, A63 (1995)
[17] J. Heindl, W. Dorsch, H. P. Strunk, St. G. Muller, R. Eckstein, D. Hofmann and A. Winnacker, Phys. Rev. Lett. **80**, 740 (1998)
[18] W. M. Vetter and M. Dudley, J. Appl. Cryst. **35**, 689 (2002)
[19] W. Wang, M. Dudley, J. C. H. Carter, V. F. Tsvetskov and C. Fazi, Mat. Res. Soc. Symp. Proc. **375**, 281 (1995)
[20] W. Si, M. Dudley, R. Glass, V. Tsetskov and J. C. H. Carter, Mater. Sci. Forum **264-268**, 429 (1998)
[21] X. Huang, M. Dudley, W. M. Vetter, W. Huang, S. Wang and C. H. Carter, Jr. Appl. Phys. Lett. **74**, 353 (1999)
[22] M. Dudley, X. Huang, W. Huang, A. Powell, S. Wang, P. Neudeck and M. Skowronski, Appl. Phys. Lett. **75**, 784 (1999)
[23] J. Giocondi, G. S. Rohrer, M. Skowronski, V. Balakrishna, G. Augustine, H. M. Hobggod and R. H. Hopkins, J. Cryst. Growth **181**, 351 (1997)
[24] T. A. Kuhr, E. K. Sanchez, M. Skowronski, W. M. Vetter and M. Dudley, J. Appl. Phys. **89**, 4625 (2001)
[25] O. Filip, B. Epelbaum, M. Bickermann and A. Winnacker, J. Cryst. Growth **271**, 142 (2004)
[26] Y. Chen, Ph. D. thesis, State University of New York at Stony Brook (2008)
[27] S. Ha, P. Mieszkowski, M. Skowronski and L. B. Rowland, J. Cryst. Growth **244**, 257 (2002)
[28] S. Ha, N. T. Nufher, G. S. Rohrer, M. D. Graef and M. Skowronski, J. Eletron. Mater. **29**, L5 (2000)
[29] M. Skowronski, J. Q. Liu, W. M. Vetter, M. Dudley, C. Hallin and H. Lendenmann, J. Appl. Phys. **92**, 4699 (2002)

[30] P. Pirouz and J. W. Yang, Ultramicroscopy **51**, 189 (1993)
[31] M. H. Hong, A. V. Samant and P. Pirouz, Phil. Mag. A **80**, 919 (2000)
[32] W. M. Vetter and M. Dudley, Mater. Sci. Eng. B **87**, 173 (2001)
[33] D. Hull and D. J. Bacon, Introduction to Dislocations, 4th Edition, Butterworth Heinemann, pp.87
[34] S. Ha, M. Skowronski and H. Lendenmann, J. Appl. Phys. **96**, 393 (2004)
[35] J. P. Bergman, H. Lendenmann, P. A. Nilsson and P. Skytt, Mater. Sci. Forum **353-356**, 299 (2001)
[36] R. E. Stahlbush, M. Fatemi, J. B. Fedison, S. D. Arthur, L. B. Rowland and S. Wang, J. Electron. Mater. **31**, 827 (2002)
[37] B. Raghothamachar, G. Dhanaraj, J. Bai and M. Dudley, Mircrosc. Res. Tech., **69**, 343 (2006)
[38] S. Wang, Ph. D. thesis, State University of New York at Stony Brook (1995)
[39] S. Ha, M. Skowronski, W. M. Vetter and M. Dudley, J. Appl. Phys. **92**, 778 (2002)
[40] K. Koga, Y. Fujikawa, Y. Ueda and T. Yamaguchi, Springer Proc. Phys. **71**, 96 (1992)
[41] H. Chen, B. Raghothamachar, W. Vetter, M. Dudley, Y. Wang, and B. Skromme, Mater. Res. Soc. Symp. Proc. **911**, B12-03 (2006)
[42] Y. Chen, G. Dhanaraj, W. Vetter, R. Ma, and M. Dudley, Mater. Sci. Forum **556-557,** 231 (2007)
[43] P. G. Neudeck and J. A. Powell, IEEE Electron Device Lett. **15,** 63 (1994)
[44] P. G. Neudeck, W. Huang, and M. Dudley, Solid-State Electron. **42,** 2157 (1998)
[45] Y. Chen, G. Dhanaraj, M. Dudley, H. Zhang, R. Ma, Y. Shishkin, and S. Saddow, Mater. Res. Soc. Symp. Proc. **911,** B09-04 (2006)
[46] J. Takahashi, M. Kanaya and Y. Fujiwara, J. Cryst. Growth **135**, 61 (1994)
[47] H. Matsunami, Physica B. **185**, 65 (1993).
[48] H. Jacobson, J. P. Bergman, C. Hallin, E. Janzen, T. Tuomi and H. Lendenmann, J. Appl. Phys. **95**, 1485 (2004).
[49] T. Ohno, H. Yamaguchi, S. Kuroda, K. Kojima, T. Suzuki and K. Arai, J. Cryst. Growth **260**, 209 (2004).
[50] H. Tsuchida, I. Kamata and M. Nagano, J. Cryst. Growth **306**, 254 (2005).
[51] X. Huang, M. Dudley, W.M. Vetter, W. Huang, W. Si and C.H. Carter Jr: J. Appl. Cryst. **32**, 516 (1999).
[52] P. Pirouz, M. Zhang, J.L. Dement and H.M. Hobgood: J. Appl. Phys. **93**, 3279 (2003).
[53] H. Tsuchida, I. Kamata and M. Nagano, Mater. Sci. Forum **600-603**, 267 (2009).
[54] Z. Zhang and T.S. Sudarshan, Appl. Phys. Lett. **87**, 151913 (2005).
[55] H. Chen, G. Wang, Y. Chen, X. Jia, J. Bai and M. Dudley, Mater. Res. Soc. Symp. Proc. **0911**-B05-24 (2006).
[56] St. G. Muller, J. J. Sumakeris, M. F. Brady, R. C. Glass, H. M. Hobgood, J. R. Jenny, R. Leonard, D. P. Malta, M. J. Paisley, A. R. Powell, V. F. Tsvetkov, S. T. Allen, M. K. Das, J. W. Palmour and C. H. Carter, Jr., Eur. Phys. J. Appl. Phys. **27**, 29 (2004)
[57] J. J. Sumakeris, J. P. Bergman, M. K. Das, C. Hallin, B. A. Hull, E. Janzen, H. Lendenmann, M. J. O'Loughlin, M. J. Paisley, S.Ha, M. Skowronski, J. W. Palmour and C. H. Carter, Jr., Mater. Sci. Forum **527-529**, 141 (2006).
[58] R E. Stahlbush, B. L. VanMil, R. L. Myers-Ward, K-K. Lew, D. K. Gaskill, C. R. Eddy, Jr., Appl. Phy. Lett. (in-press).

[59] R. E. Stahlbush**,** B. L. VanMil, K. X. Liu, K. K. Lew, R. L. Myers-Ward, D. K. Gaskill, C.R. Eddy, Jr., X. Zhang and M. Skowronski, Mater. Sci. Forum **600-603**, 317 (2009).
[60] S. Ha, H. J. Chung, N. T. Nuhfer and M. Scowronski, J. Cryst. Growth **262**, 130 (2004).
[61] R. E. Stahlbush, K. X. Liu, Q. Zhang and J. J. Sumakeris, Mater. Sci. Forum **556-557**, 295 (2007).
[62] X. Zhang, S. Ha, Y. Hanlumnyang, C. H. Chou, V. Rodriguez, M. Skowronski, J. J. Sumakeris, M. J. Paisley and M. J. O'Loughlin, J. Appl. Phys. **101**, 053517 (2007).
[63] Z. Zhang, R. E. Stalbush, P. Pirouz and T. S. Sudarshan, J. Electr. Mater. **36**, 539 (2007).
[64] X. Zhang, M. Skowronski, K. X. Liu, R. E. Stahlbush, J. J. Sumakeris, M. J. Paisley and M. J. O'Loughlin, J. Appl. Phys. **102**, 093520 (2007).
[65] H. Tsuchida, I. Kamata, K. Kojima, K. Momose, M. Odawara, T. Takahashi, Y. Ishida and K. Matsuzawa, Mater. Res. Soc. Symp. Proc. **1069**-D04-03 (2008).
[66] A. Seeger, in "*Dislocations and Mechanical Properties of Crystals*", Editors: J. C. Fisher, W. G. Johnson, R. Thomson, and T. Vreeland, Jr., John Wiley & Sons Publication, New York, 1956, pp. 252.
[67] J. W. Matthews and A. E. Blakeslee, J. Cryst. Growth **27**, 118 (1974).
[68] A. R. Lang and A. P. W. Makepeace, J. Synchrotron. Rad. **3**, 313 (1996)